Inorganic Chemistry

pubs.acs.org/IC

Article

Spectroscopic and Magnetic Studies of Co(II) Scorpionate Complexes: Is There a Halide Effect on Magnetic Anisotropy?

Laxmi Devkota,[#] Daniel J. SantaLucia,[#] Amelia M. Wheaton, Alexander J. Pienkos, Sergey V. Lindeman, J. Krzystek, Mykhaylo Ozerov, John F. Berry, Joshua Telser,* and Adam T. Fiedler*

Cite This: *Inorg. Chem.* 2023, 62, 5984–6002

Read Online

ACCESS | Metrics & More | Article Recommendations | Supporting Information

ABSTRACT: The observation of single-molecule magnetism in transition-metal complexes relies on the phenomenon of zero-field splitting (ZFS), which arises from the interplay of spin−orbit coupling (SOC) with ligand-field-induced symmetry lowering. Previous studies have demonstrated that the magnitude of ZFS in complexes with 3d metal ions is sometimes enhanced through coordination with heavy halide ligands (Br and I) that possess large free-atom SOC constants. In this study, we systematically probe this "heavy-atom effect" in high-spin cobalt(II)−halide complexes supported by substituted hydrotris(pyrazol-1-yl)borate ligands ($Tp^{tBu,Me}$ and $Tp^{Ph,Me}$). Two series of complexes were prepared: $[Co^{II}X(Tp^{tBu,Me})]$ (**1-X**; X = F, Cl, Br, and I) and $[Co^{II}X(Tp^{Ph,Me})(Hpz^{Ph,Me})]$ (**2-X**; X = Cl, Br, and I), where $Hpz^{Ph,Me}$ is a monodentate pyrazole ligand. Examination with dc magnetometry, high-frequency and -field electron paramagnetic resonance, and far-infrared magnetic spectroscopy yielded axial (D) and rhombic (E) ZFS parameters for each complex. With the exception of **1-F**, complexes in the four-coordinate **1-X** series exhibit positive D-values between 10 and 13 cm^{-1}, with no dependence on halide size. The five-coordinate **2-X** series exhibit large and negative D-values between −60 and −90 cm^{-1}. Interpretation of the magnetic parameters with the aid of ligand-field theory and *ab initio* calculations elucidated the roles of molecular geometry, ligand-field effects, and metal−ligand covalency in controlling the magnitude of ZFS in cobalt−halide complexes.

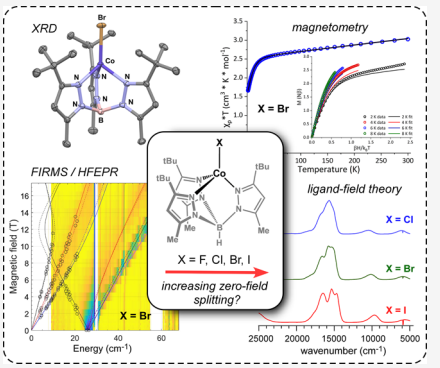

INTRODUCTION

The miniaturization of magnets to the molecular or atomic level is desirable for next-generation information storage and quantum computing applications.[1,2] One promising approach is the development of molecules, known as single-molecule magnets (SMMs),[3−5] that exhibit slow magnetic relaxation due to a large energetic barrier to the inversion of electronic spin, S. The height of the barrier is governed by the orientation energy dependence (or anisotropy) of the magnetic dipole moment. For $S > 1/2$ complexes, magnetic anisotropy is described phenomenologically using the concept of zero-field splitting (ZFS),[6−10] in which the $2S + 1$ spin sublevels (defined by m_S) are split even in the absence of a magnetic field. SMM behavior is most pronounced in complexes with large and negative (easy-axis) anisotropy, as quantified by the axial ZFS parameter D in the spin-Hamiltonian.[11,12] Coordination chemists have therefore sought to increase the magnitude of ZFS by modifying the molecular structures and electronic features of transition-metal and lanthanide complexes,[5,13−16] with the ultimate aim of generating affordable SMMs capable of operating at temperatures suitable for technological applications.

The magnetic anisotropy of complexes with nondegenerate ground states is largely mediated by second-order spin−orbit coupling (SOC), which facilitates mixing between the ground state and low-lying excited states. Because SOC is a relativistic effect that exhibits an approximate Z^4 dependence,[17] one possible strategy for increasing magnetic anisotropy involves the use of ligands that feature heavy main-group elements ($Z > 30$) as donor atoms. In this scenario, the relatively weak SOC of 3d transition-metal ions may be amplified through (partial) covalent bonding to heavy-atom donors with much larger SOC constants.[18−20] Such "heavy-atom effects" have been shown to enhance SOC-dependent photophysical processes, such as intersystem crossings between singlet and triplet states.[21] In the realm of molecular magnetism, several groups have sought to increase the magnetic anisotropy of transition-metal complexes through the incorporation of heavy-atom donors.[22,23] The effectiveness of this approach has been demonstrated in multiple studies of M−X complexes (where X = Cl, Br, and I), which found that the magnitude of ZFS increases with halide size.[24−31] However, this correlation is not always observed.[32−34] To increase metal−ligand covalency, 3d

Received: December 21, 2022
Published: March 31, 2023

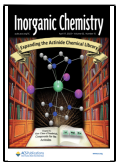

https://doi.org/10.1021/acs.inorgchem.2c04468
Inorg. Chem. 2023, 62, 5984−6002

complexes have also been prepared using ligands that feature more electropositive donor atoms from group 14 (Ge, Sn),[22,35,36] group 15 (As, Sb),[37,38] and group 16 (Se, Te).[39−42] This strategy has yielded mixed results, as the impact of the heavy-atom donors on |*D*|-values is sometimes modest.[36] It is also challenging to ascertain if changes in anisotropy are due to heavy-atom effects or subtle changes in the ligand field, which is also a major contributor to magnetic anisotropy. Therefore, quantum chemical calculations are usually necessary to distinguish between various contributions to magnetic anisotropy within a given series of complexes.[15,43]

High-spin Co(II) complexes (S = 3/2), which possess substantial magnetic anisotropy[44−49] and rich spectroscopic features,[50−54] are ideal systems for exploring heavy-atom effects. Studies of the four-coordinate $[Co^{II}X_2(EPh_3)_2]$ series (E = P, As, and Sb) have revealed a strong correlation between *D*-values and donor-atom size, although ligand-field effects are partially responsible for this trend.[37,38] Similarly, studies of $[Co^{II}(EPh)_4]^{2-}$ (E = O, S, Se) concluded that the increase in ZFS across the series is largely due to the weaker ligand fields of the heavy-atom donors, not their larger SOC constants.[15,39] More recently, Freedman and co-workers examined the magnetic properties of $[Co^{II}(Tp^{Ph,Me})(GePh_3)]$ and $[Co^{II}(Tp^{Ph,Me})(SnPh_3)]$, where $Tp^{Ph,Me}$ is hydrotris(3-phenyl-5-methylpyrazol-1-yl)borate.[22] Using ligand-field theory (LFT), it was shown that the larger *D*-value of the Sn complex (11.9 cm^{-1} vs 3.9 cm^{-1} for the Ge complex) is due to enhanced SOC from the heavy-atom effect.

These literature reports highlight the inherent challenges and complexities of using heavy-atom donors to increase the magnetic anisotropy of Co(II) complexes. Additional fundamental and systematic studies are therefore required to gauge the relative impact of molecular geometry, ligand-field effects, and SOC in controlling the sign and magnitude of *D*-values. Such magnetostructural correlations have relevance beyond molecular magnetism, as Co(II) ions are often used as spectroscopic probes for otherwise "silent" Zn(II) enzymes (*e.g.*, metallo-β-lactamases).[55,56] To this end, we report here the synthesis, structural characterization, spectroscopic features, and magnetic properties of four-coordinate $[Co^{II}X(Tp^{tBu,Me})]$ complexes (**1-X**; X = F, Cl, Br, and I), where $Tp^{tBu,Me}$ is a sterically hindered scorpionate ligand (Scheme 1). Like the Freedman complexes described above, the members of this series vary by a single axial donor atom that lies along the molecular C_3 axis of symmetry. In addition, we have prepared a related series of five-coordinate complexes with the formula $[Co^{II}X(Tp^{Ph,Me})(Hpz^{Ph,Me})]$ (**2-X**; X = Cl, Br, and I), where $Hpz^{Ph,Me}$ is a monodentate pyrazole ligand (Scheme 1). The **2-X** complexes possess distorted trigonal bipyramidal geometries in which the halide donor resides in the equatorial plane.

The spin-Hamiltonian parameters of each complex have been evaluated using variable-temperature dc magnetometry, high-frequency and -field electron paramagnetic resonance (HFEPR) spectroscopy,[57−59] and far-infrared magnetic spectroscopy (FIRMS).[42,60,61] The latter technique permitted direct measurements of magnetic anisotropy even for complexes with very large ZFS (|*D*| > 60 cm^{-1}).[54] The experimental data are interpreted within theoretical frameworks based on LFT and *ab initio* calculations. The results shed light on the conditions required for observation of a heavy-atom effect in Co(II) complexes with halide ligands, as well as the role of molecular geometry in controlling the magnetic anisotropy of Co(II) ions in synthetic and biological environments.

Scheme 1. Structures of 1-X and 2-X Complexes

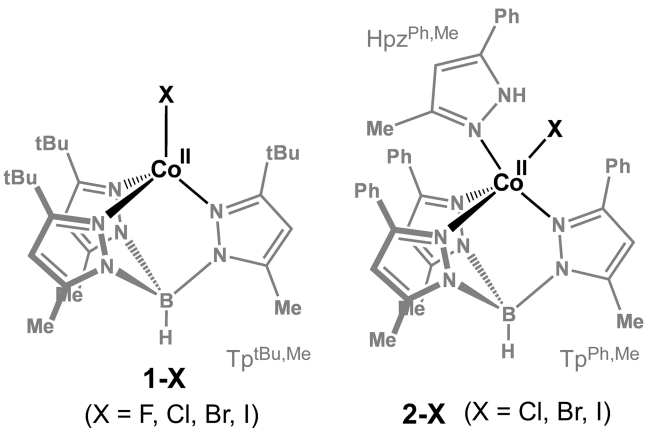

RESULTS AND ANALYSIS

Synthesis and X-ray Structures. As summarized in Scheme 2, the four-coordinate $[Co^{II}X(Tp^{tBu,Me})]$ complexes (**1-X**; X = Cl, Br, and I) were prepared by the reaction of CoX_2 salts with $K(Tp^{tBu,Me})$ in THF. Ligand metathesis by treatment of $[Co^{II}Cl(Tp^{tBu,Me})]$ (**1-Cl**) with thallium(I) fluoride in toluene yielded the fluoride complex, $[Co^{II}F(Tp^{tBu,Me})]$ (**1-F**). Syntheses of the five-coordinate complexes, $[Co^{II}X(Tp^{Ph,Me})(Hpz^{Ph,Me})]$ (**2-X**; X = Cl, Br, and I), required the prior formation of $[Co^{II}X(Tp^{Ph,Me})]$ precursors. Uehara and Akita had previously reported the synthesis of $[Co^{II}Cl(Tp^{Ph,Me})]$ by reaction of $CoCl_2$ with $K(Tp^{Ph,Me})$ in CH_3OH,[62] and this procedure also proved effective in generating the novel Br and I analogues using $CoBr_2$ and CoI_2, respectively. Subsequently, **2-Cl** was prepared by treating $[Co^{II}Cl(Tp^{Ph,Me})]$ with one equivalent of $Hpz^{Ph,Me}$ in the presence of a catalytic amount of NEt_3. Attempts to prepare the five-coordinate Br and I analogues using the same procedure caused decomposition of the $Tp^{Ph,Me}$ scorpionate instead. However, we were able to prepare **2-Br** and **2-I** by performing the reaction in the absence of a base in CH_3OH (Scheme 2).[53]

Crystals suitable for X-ray diffraction studies were grown for each complex using methods described in the Experimental section. Key metric parameters from the resulting crystal structures are summarized in Table 1. The structures of **1-Cl** and **2-Cl** are identical to those previously published by Telser[63] and Cohen,[53] respectively; the remaining structures are reported here for the first time. Complexes in the **1-X** series share distorted tetrahedral geometries with either actual or pseudo C_{3v} symmetry, as evident in the representative structure of **1-Br** shown in Figure 1. Crystals of **1-Cl** belong to the trigonal $R3c$ space group, and the Co−Cl bond lies along a crystallographic threefold axis of symmetry, resulting in equivalent Co−N_{Tp} bond distances of 2.023(2) Å and Cl−Co−N_{Tp} angles of 121.42(5)°. Other members of the **1-X** series possess lower crystallographic symmetry, and the pyrazole donors of the $Tp^{tBu,Me}$ ligands are inequivalent. Deviations from ideal C_{3v} geometry increase with the size of the halide ligand (F ≪ Br < I). Moreover, the unit cells of both **1-Br** and **1-I** consist of two symmetry-independent Co(II) complexes (labeled A and B) with slightly different metric parameters (Table 1). The Co−N_{Tp} bond distances are quite

https://doi.org/10.1021/acs.inorgchem.2c04468
Inorg. Chem. 2023, 62, 5984−6002

Scheme 2. Synthetic Routes to 1-X and 2-X Complexes

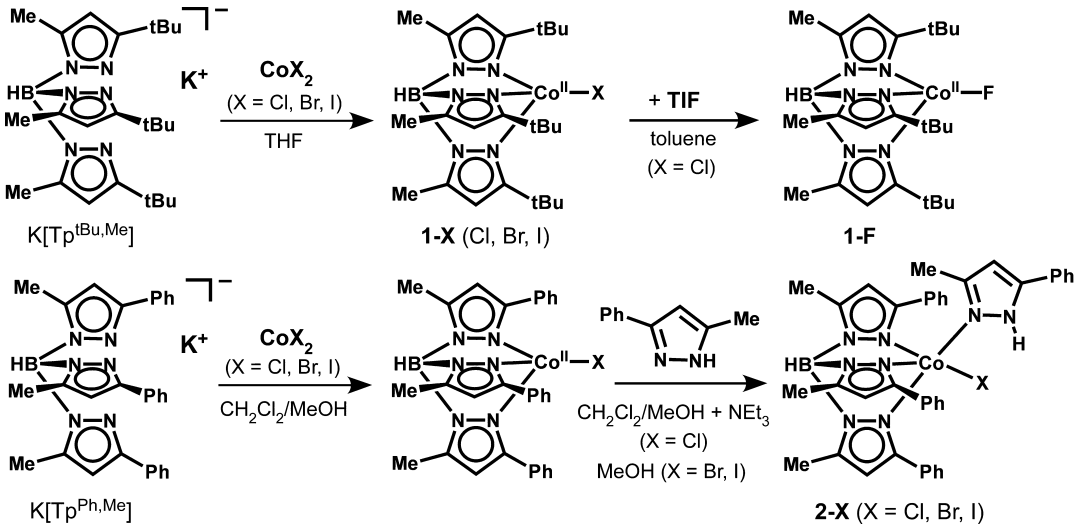

Table 1. Selected Bond Lengths (Å) and Bond Angles (°) for [CoX(Tp^{tBu,Me})] Complexes (1-X)

	[CoF(Tp^{tBu,Me})] (**1-F**)	[CoCl(Tp^{tBu,Me})] (**1-Cl**)[a]	[CoBr(Tp^{tBu,Me})] (**1-Br**)[b]		[CoI(Tp^{tBu,Me})] (**1-I**)[b]	
			A	B	A	B
Co1–X1	1.832(3)	2.2177(8)	2.3687(9)	2.3675(9)	2.5723(9)	2.5709(9)
Co–X (ave)[c]	2.060[d]	2.20	n.a.		2.54	
Co1–N_{Tp}	2.038(3)	2.0226(16)	2.052(4)	2.053(4)	2.063(5)	2.018(5)
	2.031(3)		2.022(4)	2.034(4)	2.009(5)	2.039(5)
	2.028(3)		2.051(4)	2.031(4)	2.066(5)	2.053(5)
X1–Co1–N_{Tp}	123.32(11)	121.42(5)	118.76(12)	117.68(12)	118.75(13)	120.85(13)
	121.76(11)		125.97(12)	121.31(12)	126.23(13)	124.16(14)
	121.05(11)		119.46(12)	124.18(12)	118.61(14)	117.42(14)
N_{Tp}–Co1–N_{Tp}	93.28(11)	95.30(6)	95.18(17)	97.77(17)	99.2(2)	92.4(2)
	95.10(11)		92.17(17)	96.81(17)	92.0(2)	99.9(2)
	95.00(11)		98.11(17)	92.87(16)	95.7(2)	96.2(2)
τ_4-values[e]	0.82	0.83	0.81	0.81	0.82	0.82

[a]The structure of **1-Cl** was originally reported by Telser *et al.* (ref 63). [b]The structures of **1-Br** and **1-I** contain two symmetry-independent structures (labeled A and B) in each unit cell. [c]Average of Co–X bond lengths in previously published structures of four-coordinate Tp-based complexes (n.a. = not available due to lack of structures). [d]Only one CoTpF structure has been reported to date (ref 68). [e]The definition of the τ_4-parameter is provided in ref 64.

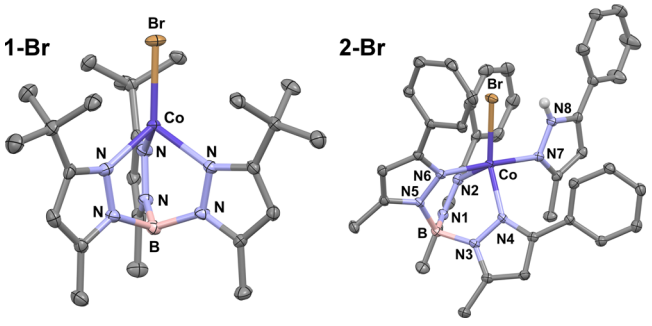

Figure 1. Thermal ellipsoid plots (50% probability) derived from X-ray crystal structures of **1-Br** (left) and **2-Br** (right). Most H-atoms are omitted for clarity, with the exception of the H-atom involved in a hydrogen bond in **2-Br**.

consistent across the **1-X** series, with an average value of 2.036 ± 0.016 Å. The average X–Co–N_{Tp} bond angle is 121.3°, while the N_{Tp}–Co–N_{Tp} bond angles are considerably smaller (average value of 95.4°). The deviation of both sets of bond angles from the ideal value of 109.5° for tetrahedral geometries is due to constraints imposed upon the pyrazolyl donors by the scorpionate framework.

As expected, the observed Co–X bond lengths in the **1-X** series increase with halide size, ranging from 1.83 Å for **1-F** to 2.57 Å for **1-I**. Table 1 compares these values to the average of Co–X bond distances found in the Cambridge Structural Database (CSD) for four-coordinate Tp-supported Co(II) complexes. While TpCoCl structures are rather abundant (22 in the CSD), there are far fewer TpCoI structures (five total[65−67]) and only a single TpCoF structure.[68] Interestingly, there are no prior reports of TpCoBr structures in the CSD. The absence of published crystallographic studies of TpCoBr complexes is surprising given that structures of analogous complexes with fluoro, chloro, and iodo ligands have been known since the 1990s. The Co–X bond lengths of **1-Cl** and **1-I** are close to the literature averages, albeit longer by 0.02–0.03 Å (Table 1). In contrast, the Co–F distance of **1-F** (1.832 Å) is dramatically shorter than the value of 2.060 Å reported by Parkin for the closely related complex, [Co^{II}F(Tp^{tBu,H})].[68] The magnitude of this difference (0.23 Å) is striking, as the structures are otherwise very similar. Comparison to analogous

https://doi.org/10.1021/acs.inorgchem.2c04468
Inorg. Chem. 2023, 62, 5984−6002

$Tp^{tBu,Me}$-based Fe−F and Zn−F complexes revealed M−F bond lengths of 1.859 and 1.813 Å,[69,70] respectively, which are consistent with the shorter value reported here for **1-F**. We hypothesize that the earlier structure is contaminated by a significant amount of the precursor complex, $[Co^{II}Cl(Tp^{tBu,H})]$, which causes the Co−F bond to appear artificially long, a crystallographic effect that was systematically examined in other compounds by Parkin.[71]

The five-coordinate Co(II) complexes (**2-X**) exhibit distorted trigonal bipyramidal geometries, as reflected in τ-values between 0.55 and 0.63 (Table 2).[72] In contrast to the C_{3v} symmetry of the **1-X** series, members of the **2-X** series are devoid of symmetry elements. The monodentate pyrazole ligand ($Hpz^{Ph,Me}$) occupies an axial position trans to one of the Tp-based pyrazolyl donors. The orientation of the $Hpz^{Ph,Me}$ ligand minimizes steric repulsion by pointing its Ph substituent away from the Co center, while the Me group lies in a cleft between two Ph rings of $Tp^{Ph,Me}$ (Figure 1). This arrangement also allows the $Hpz^{Ph,Me}$ ligand to engage in $\pi-\pi$ stacking interactions with a nearby Ph group of the $Tp^{Ph,Me}$ scaffold.[73] The halide ligand lies in the equatorial plane and participates in a hydrogen-bonding interaction with the NH unit of $Hpz^{Ph,Me}$. The increase in coordination number as well as the intramolecular hydrogen bond are accompanied by an elongation of ∼0.10 Å in Co−X bond distances relative to the **1-X** congeners. The Co−N_{Tp} bonds are also longer in the five-coordinate complexes, although the change is not uniform. Distances for the two equatorial Co−N_{Tp} bonds lie between 2.06 and 2.09 Å, whereas the longer axial Co−N_{Tp} bonds range from 2.21 Å (**2-Cl**) to 2.30 Å (**2-I**). As described below, these structural distortions have a major impact on the magnetic and spectroscopic properties of the **2-X** series.

Table 2. Selected Bond Lengths (Å) and Bond Angles (°) for $[Co^{II}X(Tp^{Ph,Me})(Hpz^{Ph,Me})]$ (2-X)

	$[CoCl(Tp^{Ph,Me})(Hpz^{Ph,Me})]$ **2-Cl**[a]	$[CoBr(Tp^{Ph,Me})(Hpz^{Ph,Me})]$ **2-Br**	$[CoI(Tp^{Ph,Me})(Hpz^{Ph,Me})]$ **2-I**
Co1−X1	2.3203(4)	2.4750(3)	2.6646(6)
Co1−N2	2.0738(12)	2.0885(14)	2.059(3)
Co1−N4	2.0853(13)	2.0750(13)	2.066(3)
Co1−N6	2.2082(13)	2.2149(14)	2.299(3)
Co1−N7	2.1409(13)	2.1418(14)	2.153(3)
N2−Co−X1	143.83(4)	120.32(4)	136.11(9)
N4−Co−X1	120.51(4)	144.12(4)	128.35(9)
N6−Co−X1	90.52(3)	90.34(4)	93.73(8)
N7−Co−X1	90.51(4)	91.37(4)	92.45(1)
N2−Co−N4	94.88(5)	94.75(5)	95.20(13)
N2−Co−N6	82.76(5)	88.83(5)	82.62(12)
N2−Co−N7	95.50(5)	92.11(5)	93.52(13)
N4−Co−N6	88.26(5)	82.46(5)	86.36(12)
N4−Co−N7	92.56(5)	94.93(5)	89.12(12)
N6−Co−N7	178.14(5)	177.29(5)	173.76(12)
τ[b]	0.57	0.55	0.63

[a]Structure was originally reported in ref 53.[53] [b]A five-coordinate complex with the ideal square-pyramidal geometry would have a τ-value of 0.0, while those with the ideal trigonal bipyramidal geometry would have a value of 1.0.[72]

Magnetic Susceptibility Studies. Magnetic susceptibility, χ_p, was determined for solid-state samples of the four- and five-coordinate Co(II) complexes with a dc applied field. Data measured for **1-F** and **1-Cl** are shown in Figure 2, and data collected for **1-Br** and **1-I** are provided in Figures S1 and S2. Similar magnetic susceptibilities are observed across the **1-X** series; in each case, there is a steep downturn in $\chi_P T$ at low temperatures due to ZFS. The downturn in $\chi_P T$ occurs at a lower temperature in **1-F** (∼15 K) than the other **1-X** complexes (∼30 K), which suggests that the ZFS in **1-F** is smaller than for the other **1-X** complexes. The $\chi_P T$ values at 300 K for the **1-X** complexes are 2.21, 3.03, 3.03, and 3.20 cm^3 K mol^{-1} for **1-F**, **1-Cl**, **1-Br**, and **1-I**, respectively, which are much larger than the expected spin-only value of an $S = 3/2$ system (1.876 cm^3 K mol^{-1}). Such discrepancies between the observed and spin-only expectation values are commonly observed for monometallic high-spin Co(II) systems, which possess substantial unquenched orbital angular momentum.[4,9,10,46,48,54] The slight linear increase of $\chi_P T$ in the high temperature regime (T > 50 K) in each plot is due to temperature-independent paramagnetism (TIP), which arises from coupling of the magnetic ground state to low-lying excited states and/or from small amounts of metallic sample impurities.

The **1-X** complexes were modeled using an $S = 3/2$ spin Hamiltonian with axial g-values and ZFS parameters; the

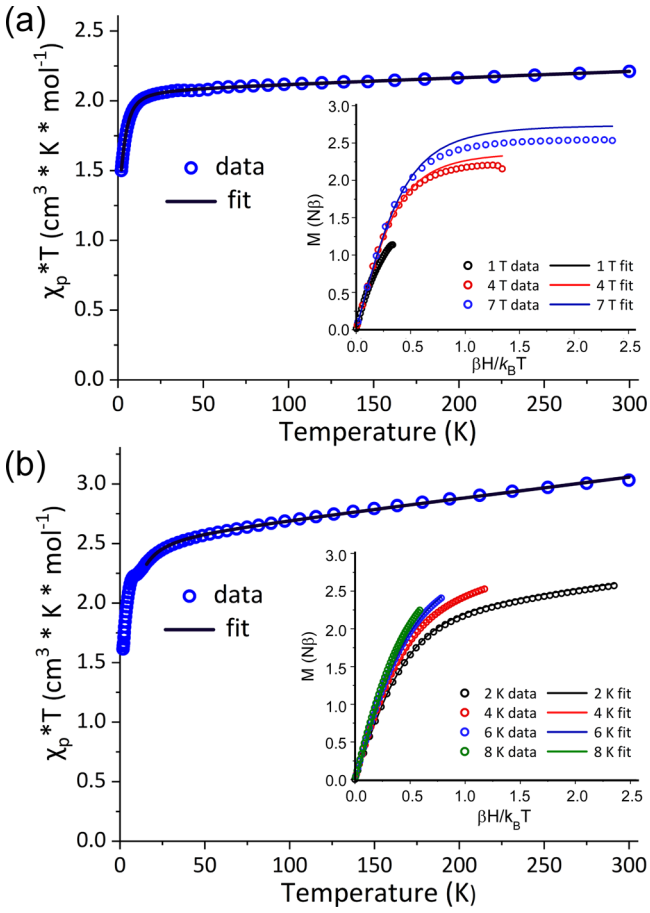

Figure 2. (a) DC magnetic susceptibility of **1-F** with data points from 1.8 to 300 K. The inset displays variable-temperature fixed-field (VTVH) magnetization isofield measurements at 1, 4, and 7 T. (b) DC magnetic susceptibility of **1-Cl** with data points from 1.8 to 300 K. The inset displays variable-field fixed-temperature (VHVT) magnetization isotherms measured at 2, 4, 6, and 8 K. The solid lines correspond to spin-Hamiltonian models generated by simultaneous fits to both the susceptibility and VTVH/VHVT data, as described in the text. Fit parameters are provided in Table 3.

https://doi.org/10.1021/acs.inorgchem.2c04468
Inorg. Chem. 2023, 62, 5984−6002

Table 3. Summary of Fitting Parameters for Magnetic Susceptibility Data Collected for 1-X and 2-X Series of Co(II) Complexes

	1-F	1-Cl	1-Br	1-I
$g_{\parallel}$	$g_{z/y}$ = 2.335(2)	2.412(4)	2.200(5)	2.314(7)
$g_{\perp}$	g_x = 1.808(2) $g_{y/z}$ = 2.144(5)	2.276(2)	2.376(2)	2.394(2)
D (cm^{-1})	±3.63(5)[b]	+9.08(4)	+12.6(1)	+9.35(7)
E/D	0.333	0.000	0.000	0.000
TIP (cm^3 mol^{-1})	0.000429(5)	0.00178(1)	0.00172(1)	0.00197(1)
residual[a]	0.0000828	0.000163	0.0189	0.0178
	2-Cl	**2-Br**	**2-I**	
$g_{\parallel}$	2.6074(2)	2.7119(2)	2.7418(7)	
$g_{\perp}$	2.064(1)	2.268(2)	2.217(3)	
D (cm^{-1})	−68.9(1)	−81.7(1)	−80.9(3)	
zJ (cm^{-1})	n/a	n/a	−0.0070(2)	
TIP (cm^3 mol^{-1})	0.000368(6)	0.000414(7)	−0.00010(2)	
residual[a]	0.0000479	0.000152	0.0000141	

[a]Residual = $\left[\sum_{i=1}^{\text{points}} (M_{\text{exper}} - M_{\text{calc}})^2\right]\left[\sum_{i=1}^{\text{points}} (\chi_{\text{exper}} - \chi_{\text{calc}})^2\right]$; where $M_{\text{exper}}/M_{\text{calc}}$ = measured/calculated magnetization and $\chi_{\text{exp}}/\chi_{\text{calc}}$ = measured/calculated susceptibility. [b]The data can be modeled equally well with a positive or negative value for D. The values for g_y and g_z are swapped depending on the sign of D because the model is at the rhombic limit.

exception is **1-F**, which was modeled with rhombic parameters. The final fitting parameters are listed in Table 3. Notably, we were able to fit the susceptibility and magnetization data simultaneously for each complex. The magnitude of D for **1-F** is relatively small (±3.63(5) cm^{-1}) compared to other previously reported four-coordinate Co(II) complexes ($|D| \approx$ 10−80 cm^{-1}).[4,8,10,15] The sign of D is irrelevant for **1-F** as the anisotropy is at the rhombic limit (E/D = 0.333). The other **1-X** complexes have larger and positive D-values of +9.08 cm^{-1} (**1-Cl**), +12.6 cm^{-1} (**1-Br**), and +9.35 cm^{-1} (**1-I**).

The magnetic susceptibility data measured for **2-I**, shown in Figure 3, are representative of the **2-X** series (data for **2-Cl** and **2-Br** are provided in Figures S3 and S4). In each case, there is a steep downturn in $\chi_P T$ below ca. 100 K and either a gradual increase (for **2-Cl** and **2-Br**) or saturation (**2-I**) of the measured $\chi_P T$ values above 100 K. The observation that the downturn in $\chi_P T$ occurs at much higher temperatures in the **2-X** complexes than the **1-X** complexes suggests that the ZFS in the **2-X** complexes is much larger than in the **1-X** complexes. The $\chi_P T$ values at 300 K for all three compounds (2.57, 2.93, and 2.75 cm^3 K mol^{-1} for **2-Cl**, **2-Br**, and **2-I**, respectively) are again substantially greater than the S = 3/2 spin-only expectation value, and can be attributed to orbital contributions to the magnetic moment of the high-spin Co(II) ion. Similar to the **1-X** complexes, the slight linear increase of $\chi_P T$ for **2-Cl** and **2-Br** in the high temperature regime (>150 K) is due to TIP. The lowering of the $\chi_P T$ values below ca. 100 K, as well as the lack of nested behavior of the reduced magnetization curves, is indicative of substantial zero-field splitting (ZFS) of the Co(II) ions in the **2-X** series.

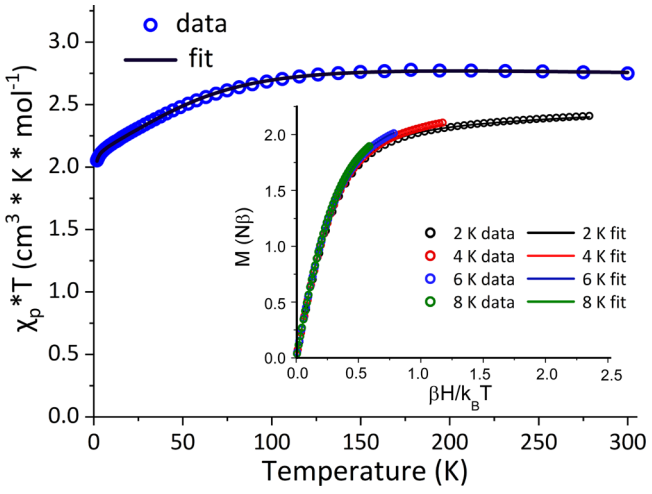

Figure 3. DC magnetic susceptibility of **2-I** with data points from 1.8 to 300 K. Inset: VHVT magnetization measurements showing 2, 4, 6, and 8 K isotherms. The solid lines correspond to the spin-Hamiltonian model generated by simultaneous fits to both the susceptibility and VHVT data, as described in the text. Fit parameters are provided in Table 3.

For all three of the **2-X** compounds, the D-values are large and negative: −68.9(1), −81.7(1), and −80.9(3) cm^{-1} for **2-Cl**, **2-Br**, and **2-I**, respectively. It is worth noting in this context that for systems with considerable contributions from SOC, the spin-only Hamiltonian model begins to break down.[8−10,13,74] In these cases, the values of D determined from spin-only models can fail to capture the full extent of single-ion anisotropy in a system.[9,74,75] This is clearly the case for the **2-X** complexes, where the presence of substantial unquenched orbital angular momentum is evident in the large deviation of g-values from the free-electron value of g = 2.0 (Table 3). Nevertheless, the magnetization data and fits unambiguously demonstrate that D-values for the **2-X** series are large and negative. As described in the next section, these results are fully consistent with the ZFS parameters derived from HFEPR and FIRMS studies, thus validating the models used in the analysis of the magnetic susceptibility data.

HFEPR and FIRMS Data. *(i) Four-coordinate series (1-X).* HFEPR studies of **1-F** yielded high-quality spectra, despite the large widths of the turning points (Figure 4, left). Although no significant field-induced orientation effects were observed in loose samples of **1-F**, a somewhat better powder pattern was obtained with a pellet sample. Observation of the inter-Kramers transition at low field provides an approximate ZFS energy of ∼270 GHz (9 cm^{-1}). This energy translates into a D'-value of 4.5 cm^{-1}, where $D' = \{D^2 + 3E^2\}^{1/2}$. Further experiments, performed at multiple frequencies according to the tunable frequency methodology[76] (Figure 5 upper left),

https://doi.org/10.1021/acs.inorgchem.2c04468
Inorg. Chem. 2023, 62, 5984−6002

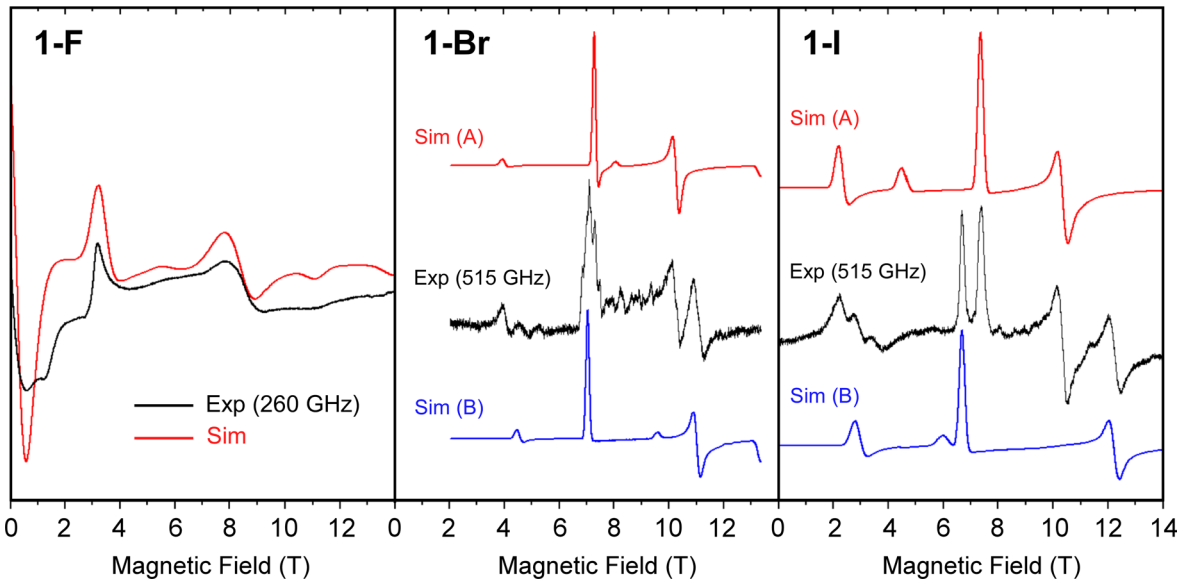

Figure 4. Low-temperature (5−10 K) high-frequency and -field EPR (HFEPR) spectra (black line) of the [$Co^{II}X(Tp^{tBu,Me}$)] (**1-X**) series with X = F at 260 GHz (left), X = Br at 515 GHz (center), and X = I at 515 GHz (right). The spectra are accompanied by simulations assuming a powder distribution and using spin-Hamiltonian parameters provided in the text and Table 4. In the case of X = Br and X = I, there are two simulations (A and B) differing by color, which correspond to the two-spin species observed in the crystallographic structures. HFEPR spectra of **1-Cl** were previously reported.[63]

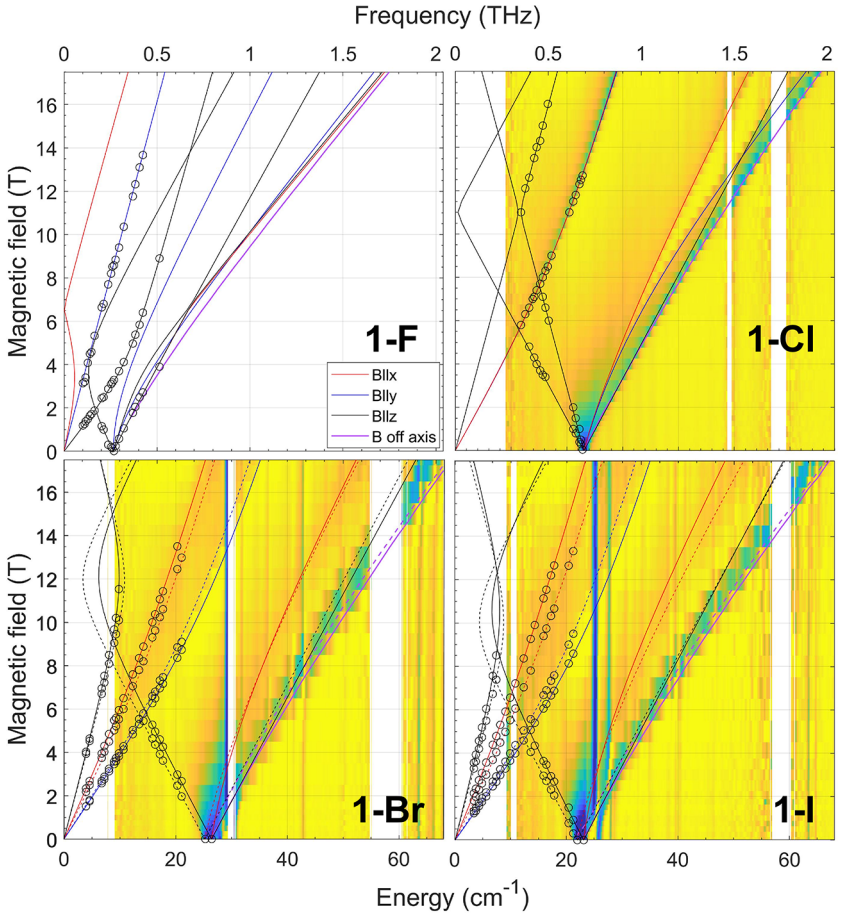

Figure 5. Combined HFEPR and far-infrared magnetic spectroscopy (FIRMS) data for the **1-X** series. FIRMS heat maps for **1-Cl**, **1-Br**, and **1-I** were collected at a low temperature (5.5 K). The spectral regions represented by a blue color indicate strong absorption of the sub-THz radiation, while the yellow regions indicate weak absorption. The circles indicate turning points observed in the corresponding HFEPR spectra. The curves are simulations of those points using the spin-Hamiltonian parameters listed in Table 4. The solid and dashed lines for **1-Br** and **1-I** represent the two-spin species (A and B) that possess slightly different spin-Hamiltonian parameters.

https://doi.org/10.1021/acs.inorgchem.2c04468
Inorg. Chem. 2023, 62, 5984−6002

Table 4. Summary of Spin-Hamiltonian Parameters for Four-Coordinate $[Co^{II}X(Tp^{tBu,Me})]$ (1-X; X = F, Cl, Br, and I) Obtained from HFEPR, FIRMS, and QCT Calculations

complex	method[a]	g_x	g_y	g_z	g_{ave}	D (cm^{-1})[b]	E (cm^{-1})[b]	$\lvert E/D\rvert$[b]	D' (cm^{-1})[c]
1-F	Exper.	2.224(2)	2.334(9)	2.317(22)	2.292	−3.86(1)	−1.258(5)	0.326	4.43
	QCT	2.258	2.299	2.280	2.279	−3.93 (−2.41)	−0.845 (−0.782)	0.215 (0.325)	4.19 (2.76)
1-Cl	Exper.	2.35(1)	2.35(1)	2.24(1)	2.313	+11.52(2)	0.141(1)	0.0122(1)	11.52
	QCT	2.383	2.380	2.222	2.328	+11.02 (+14.59)	0.140 (0.112)	0.013 (0.008)	11.02 (14.59)
1-Br	Exper.	2.32(2)	2.42(2)	2.24(2)	2.327	+12.50(2)	1.11(6)	0.09(1)	12.65
(isomer A)	QCT	2.402	2.409	2.214	2.342	+14.43 (+16.96)	0.614 (0.374)	0.043 (0.022)	14.47 (16.97)
1-Br	Exper.	2.35(1)	2.36(1)	2.27(1)	2.327	+12.84(2)	1.80(2)	0.140(2)	13.21
(isomer B)	QCT	2.404	2.432	2.213	2.350	+15.67 (+18.45)	1.83 (1.31)	0.117 (0.071)	15.99 (18.59)
1-I	Exper.	2.43(3)	2.38(2)	2.26(2)	2.357	+10.76(2)	1.15(6)	0.11(1)	10.94
(isomer A)	QCT	2.449	2.408	2.200	2.352	+17.80 (+19.68)	1.86 (1.70)	0.105 (0.086)	18.09 (19.90)
1-I	Exper.	2.30(1)	2.40(1)	2.23(1)	2.310	+11.03(2)	1.90(3)	0.172(2)	11.51
(isomer B)	QCT	2.418	2.489	2.200	2.369	+19.82 (+22.12)	3.62 (2.83)	0.182 (0.128)	20.79 (22.66)

[a]Exper. = spin-Hamiltonian parameters determined from combined HFEPR and FIRMS experiments; QCT = computed parameters derived from QCT. [b]For the computed D and E/D values, the first entry was calculated using the second-order perturbation theory, while the second entry (in parentheses) was calculated using the effective Hamiltonian approach. [c]$D' = \{D^2 + 3E^2\}^{1/2}$.

allowed us to disentangle the axial (D) and rhombic (E) contributions to ZFS. As summarized in Table 4, the following spin-Hamiltonian parameters were obtained from HFEPR: D = −3.86(1) cm^{-1}, E = −1.258(5) cm^{-1} (E/D = 0.326), $\boldsymbol{g}$ = [2.224(2), 2.334(9), 2.317(22)]. The magnitude of D and the highly rhombic nature of the ZFS tensor are fully consistent with the magnetometry data. FIRMS studies of **1-F** were not performed as the zero-field resonance appears below the detection threshold of this technique.

Complex **1-Cl** was previously studied (by some of us) using field-domain magnetic resonance spectroscopy,[63] and thus the HFEPR experiments were not repeated. From the ZFS parameters obtained in that earlier work (D = +11.52(2) cm^{-1}, $|E|$ = 0.141(1) cm^{-1}), one calculates a D'-value of 11.523 cm^{-1}. The ZFS tensor of **1-Cl** is almost fully axial (E/D = 0.012), in sharp contrast to the maximum rhombicity observed for **1-F**. Complex **1-Cl** produced a very good FIRMS response with a single zero-field transition at 23.08 cm^{-1} (Figure 5, upper right). This value corresponds to D' = 11.54 cm^{-1}, in remarkable agreement with the previous HFEPR result. The dataset from our previous study[63] was used to plot the field vs frequency dependence of the EPR turning points, which are superimposed on the FIRMS map in Figure 5.

Microcrystalline samples of **1-Br** were found to torque strongly in the magnetic field used for HFEPR investigations, so that the resulting spectra were characteristic of a field-aligned sample ("quasi-single crystal"). For an S = 3/2 spin system where it is assumed that D > 0, one expects only one resonance corresponding to the allowed transition within the m_S = ±1/2 Kramers doublet. Instead, two resonances were observed (Figure S5), consistent with the presence of two crystallographically inequivalent sites as observed by XRD (*vide supra*). After the compound was ground with *n*-eicosane and pressed into a pellet, the spectra changed radically and were more typical of powder patterns. The spectrum shown in Figure S5 (left) represents the low-frequency regime, where the only observed resonances originate from the intra-Kramers transition of the m_S = ± 1/2 doublet. Each turning point of that transition is clearly doubled, indicating the presence of two magnetically inequivalent sites with somewhat different spin-Hamiltonian parameters. Figure 4 (middle) shows the HFEPR spectrum of **1-Br** in the high-frequency regime (515 GHz), where inter-Kramers transitions between the m_S = ±1/2 and ±3/2 doublets are discernible at low magnetic fields. From these transitions, it was possible to extract D'-values of 12.65 and 13.21 cm^{-1} for the two structures of **1-Br**. A third branch of inter-Kramers resonances could also be observed at 5.4 T in the spectrum shown in Figure 4 (middle), which suggests the presence of yet a third species. However, this weak feature could not be tracked through the whole range of frequencies and its origin remains unknown.

The full set of spin-Hamiltonian parameters for the two species (A and B) were obtained through the tunable-frequency method, and the resulting values are listed in Table 4. Unlike **1-Cl**, the ZFS tensors of **1-Br** exhibit a moderate degree of rhombicity (E/D = 0.09 and 0.14 for A and B, respectively). Samples of **1-Br** also presented a very good FIRMS response with two zero-field transitions measured at 25.31 and 26.46 cm^{-1} (Figure 5, lower left), along with a weaker third transition at 27.90 cm^{-1} (Figure S6, middle). These observed transition energies correspond to D'-values of 12.66 and 13.23 cm^{-1} for the A and B sites, respectively; again, the agreement between the FIRMS and HFEPR results is nothing short of spectacular. Moreover, the ability of these techniques to accurately provide distinct sets of spin-Hamiltonian parameters for crystallographically independent structures of the same complex is impressive, as such cases are often challenging to treat in the field of molecular magnetism.

Like **1-Br**, HFEPR and FIRMS investigations of **1-I** revealed the presence of two magnetically inequivalent sites with distinct parameters. Both field-aligned and powder-type spectra exhibit doubling of the observed features (Figure S5). The inter-Kramers transitions were discernible in the low-field region of the high-frequency spectra (Figure 4), yielding D'-values of 10.94 and 11.51 cm^{-1}. Nearly identical D' energies were ascertained from the intense zero-field transitions observed by FIRMS (Figures 5 and S6). Analysis of the tunable-frequency HFEPR data yielded the set of spin-Hamiltonian parameters listed in Table 4. The ZFS values of **1-I** are somewhat smaller than those observed for **1-Br**, but the rhombicity of the former complex is more pronounced. Thus, while the ZFS tensors of **1-Cl** and **1-F** lie at the axial and rhombic limits, respectively, **1-Br** and **1-I** fall between these extremes with E/D ratios in the range of 0.09−0.17. The absolute E values for **1-F**, **1-Br**, and **1-I** are quite similar, however, with each falling between 1.10 and 1.90 cm^{-1}.

https://doi.org/10.1021/acs.inorgchem.2c04468
Inorg. Chem. 2023, 62, 5984−6002

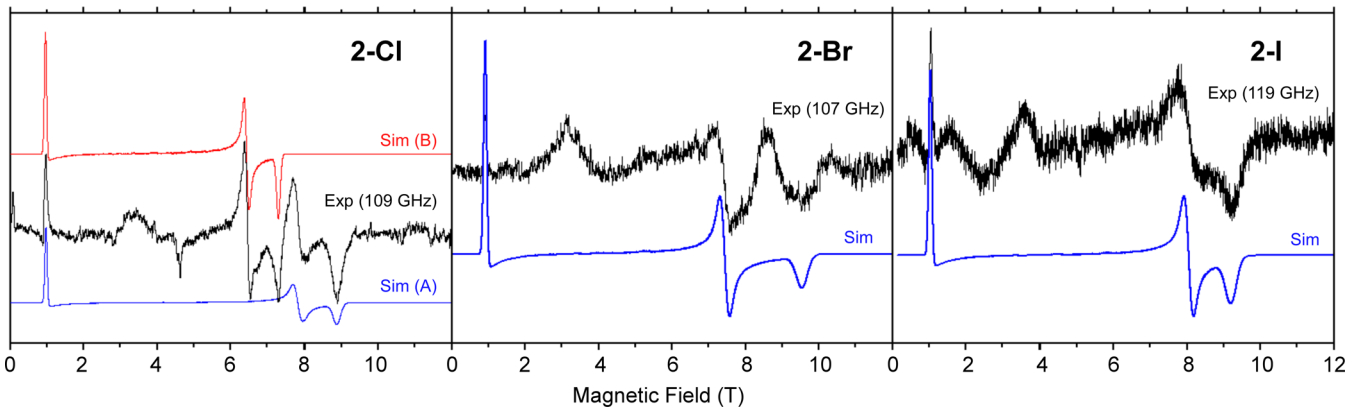

Figure 6. HFEPR spectra of the [$Co^{II}X(Tp^{Ph,Me})(Hpz^{Ph,Me})$] (**2-X**) series at 5 K (black traces). Left: **2-Cl** at 109 GHz; middle: **2-Br** at 107 GHz; right: **2-I** at 119 GHz. All of the turning points belong to the intra-Kramers transition within the $m_S = \pm 3/2$ manifold. The colored lines are simulations using the spin-Hamiltonian parameters listed in Table 5. In the case of **2-Cl**, the two different colors represent the two magnetically inequivalent complexes. The weak, broad resonances in **2-Br** and **2-I** in the 1.5−4 T range could not be identified.

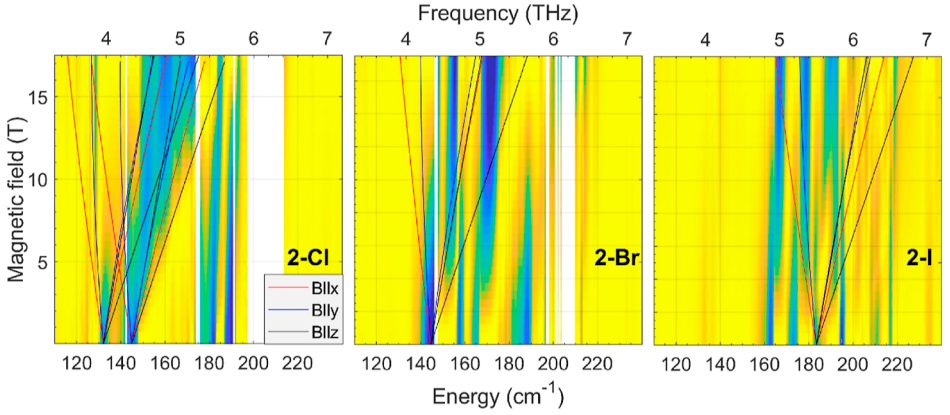

Figure 7. FIRMS heat maps measured at low temperature (5.5 K) for the five-coordinate [$Co^{II}X(Tp^{Ph,Me})(Hpz^{Ph,Me})$] series: **2-Cl** (left), **2-Br** (center), **2-I** (right). The spectral regions represented by a blue color indicate strong absorption of the THz radiation, while the yellow regions indicate weak absorption. The lines are simulations of the turning points using the spin-Hamiltonian parameters listed in Table 5.

Table 5. Summary of Spin-Hamiltonian Parameters for Five-Coordinate [$CoX(Tp^{tBu,Me})(Hpz^{Ph,Me})$] (2-X; X = Cl, Br, and I) Obtained from HFEPR, FIRMS, and QCT Calculations

complex	method[a]	g_x	g_y	g_z	D (cm^{-1})[b]	$\lvert E\rvert$ (cm^{-1})[b]	$\lvert E/D\rvert$[b]	D' (cm^{-1})[c]
2-Cl[d]	Exper. (A)	2.1	2.2	2.7	−63.9	9.59	0.15	66.0
	Exper. (B)	2.55	2.7	2.7	−70.1	10.52	0.15	72.4
	QCT	2.042	2.172	2.913	−105.2 (−73.1)	7.74 (10.4)	0.073 (0.143)	106.1 (75.3)
2-Br	Exper.	2.05	1.9	2.8	−69.6	11.14	0.16	72.2
	QCT	2.128	1.996	3.00	−142.9 (−83.7)	7.79 (11.7)	0.054 (0.139)	143.5 (86.1)
2-I	Exper.	2.50	2.55	2.75	−89.1	12.05	0.135	91.5
	QCT	2.011	2.077	3.021	−156.0 (−86.0)	8.11 (10.8)	0.052 (0.126)	156.6 (88.0)

[a]Exper. = spin-Hamiltonian parameters determined from combined HFEPR and FIRMS experiments; QCT = computed parameters derived from QCT. [b]For the computed D and E/D values, the first entry was calculated using the second-order perturbation theory, while the second entry (in parentheses) was calculated using the effective Hamiltonian approach. [c]$D' = \{D^2 + 3E^2\}^{1/2}$. [d]HFEPR spectra of **2-Cl** feature two different sets of turning points, which are attributed to magnetically distinct species.

(ii) Five-coordinate series (2-X). Each member of the **2-X** series (X = Cl, Br, and I) yielded a modest HFEPR response (Figure 6). As predicted by magnetometry, the magnitude of ZFS was too large to observe turning points belonging to the transition between Kramers doublets. Instead, only features originating from the intra-Kramers transition within the $m_S = \pm 3/2$ doublet were observed. In contrast to their congeners in the **1-X** family, all of the five-coordinate complexes possess negative D-values. This change explains the lower signal-to-noise ratio of the **2-X** spectra: the intra-Kramers transition within the $m_S = \pm 3/2$ doublet is forbidden and becomes only partially allowed through the mixing of levels induced by the rhombic parameter E. In the case of **2-Cl**, two different sets of turning points were resolved, which are attributed to magnetically distinct species. While the magnitude of ZFS could not be measured using HFEPR, the rhombicity factor (E/D) and g-values were obtained from the field/frequency maps shown in Figure S7.

FIRMS studies revealed multiple zero-field transitions in the energy range of 120−220 cm^{-1} and numerous field-dependent

https://doi.org/10.1021/acs.inorgchem.2c04468
Inorg. Chem. 2023, 62, 5984−6002

resonance modes for each member of the **2-X** series (Figures 7 and S8). Similar results were previously encountered in studies of Co(II) complexes[77] and theoretically treated for the case of a Yb(III) complex by Kragskow *et al.*[78] To briefly summarize these prior findings, in many high-spin systems where zero-field transitions have energies in the range of ∼100−500 cm^{-1}, magnetic bands exhibit strong coupling with low-energy phonons or vibrons that possess similar frequencies, resulting in multiple zero-field resonances. In such cases, the conventional spin-Hamiltonian model has limited value, and a more complex approach is required that includes spin-phonon/vibron interactions. Because this methodology is beyond the scope of this paper, we made certain assumptions to identify the inter-Kramers transition of the $S = 3/2$ spin system among the FIRMS resonances observed at zero and high field. In particular, we selected the zero-field transitions that fall closest to values obtained from magnetometry and quantum chemical theory (QCT) calculations (*vide infra*). This approach yielded the following D'-values: 66.0 and 72.4 cm^{-1} (**2-Cl**), 72.2 cm^{-1} (**2-Br**), and 91.5 cm^{-1} (**2-I**). The presence of two magnetically inequivalent **2-Cl** species, as observed in the HFEPR spectra, is also evident in the FIRMS data. The combined HFEPR and FIRMS data allowed us to resolve the five spin-Hamiltonian parameters (D, E, g_x, g_y, and g_z) for each complex, and the results are summarized in Table 5. We offer the caveat, however, that these values are not as accurate as those obtained for the four-coordinate **1-X** series and should be considered estimates only. Regardless, it is evident from the HFEPR/FIRMS experiments that the increase in coordination number from 4 → 5 has a dramatic impact on the magnitude of ZFS and the sign of D, consistent with the magnetic susceptibility data presented above.

Visible−NIR Absorption Spectra and Ligand-Field Analysis. Electronic absorption spectra were measured across the visible−NIR regions (5000−25,000 cm^{-1}) at room temperature to assess the role of ligand-field effects in modulating the magnetic properties of the Co(II) complexes. Data were collected in CH_2Cl_2 solutions at room temperature. The spectra of the four-coordinate **1-X** complexes (Figure 8) revealed a series of bands arising from ligand-field (d−d) transitions. Band energies and assignments are summarized in Table 6. The assignments are derived from previous studies of Co(II) complexes with pseudo-tetrahedral symmetry, in particular the spectral analysis of [CoCl($Tp^{tBu,R}$)] reported by Telser, Larrabee, and co-workers.[63,79] The set of peaks in the visible region (14,500−18,500 cm^{-1}) is derived from the $^4A_2 \rightarrow {}^4T_1(P)$ transition in the parent T_d symmetry. The $^4T_1(P)$ term splits into $^4A_2(P)$ and $^4E(P)$ states in C_{3v} symmetry, which are both dipole-allowed with z- and xy-polarization, respectively, and further deviation from ideal C_{3v} symmetry introduces a rhombic splitting of the $^4E(P)$ levels. The energies of the $^4A_2 \rightarrow {}^4T_1(P)$ components are therefore diagnostic of axial and rhombic distortions to the electronic geometry. As evident in Table 6, the axial splitting between the $^4A_2(P)$ and $^4E(P)$ levels changes across the **1-X** series. For **1-F**, the $^4A_2 \rightarrow {}^4E(P)$ transitions at 17,390 and 18,180 cm^{-1} are considerably higher in energy than the $^4A_2 \rightarrow {}^4A_2(P)$ transition at 15,180 cm^{-1}. The corresponding bands of **1-Cl** and **1-Br** have similar energies in the range of 15,000−17,000 cm^{-1}. In contrast, **1-I** more clearly exhibits an inverted pattern in which the $^4A_2(P)$ state is higher in energy than the $^4E(P)$ states. This reversal is caused by the decrease in σ-donating ability with

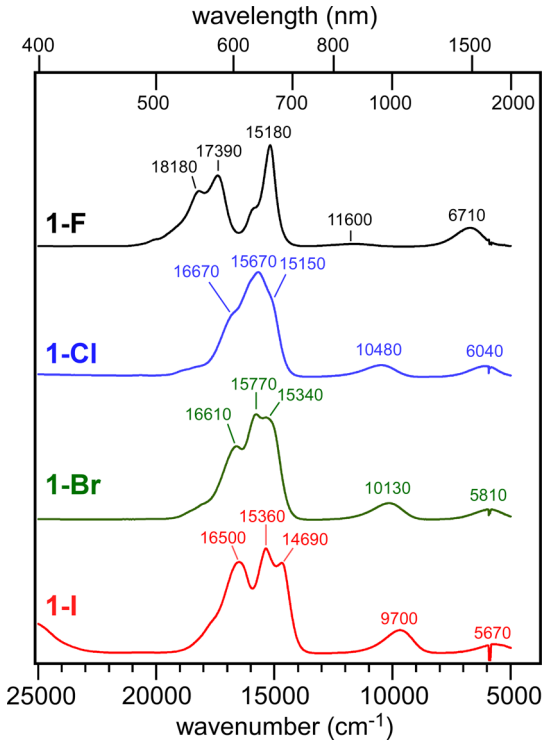

Figure 8. Electronic absorption spectra of **1-X** complexes in CH_2Cl_2 solutions at room temperature. Band intensities have been normalized to emphasize spectral similarities across the series. The energies of ligand-field transitions are indicated in wavenumbers (cm^{-1}).

increasing halide size, which lowers the relative energy of the $^4A_2 \rightarrow {}^4E(P)$ transitions (*vide infra*). The splitting between the two $^4A_2 \rightarrow {}^4E(P)$ transitions is greatest for **1-F** and **1-I**, whereas smaller values are observed for **1-Cl** and **1-Br** (Table 6). This splitting correlates with the rhombicity (E/D ratio) of the ZFS tensors measured by HFEPR, demonstrating the congruence between the electronic absorption and magnetic data.

The two observed bands in the NIR region are derived from the $^4A_2 \rightarrow {}^4T_1(F)$ transition in the parent T_d symmetry. In C_{3v} symmetry, this transition splits into $^4E(F)$ and $^4A_2(F)$ components with energies between 5500−6800 and 9700−11,600 cm^{-1}, respectively, in the **1-X** series. These bands exhibit a pronounced red shift as the size of the halide increases, consistent with the trend in ligand-field strength predicted by the spectrochemical series. The remaining ligand-field transitions, which arise from the parent $^4A_2 \rightarrow {}^4T_2(F)$ transition, are not observed due to their low energies (<5000 cm^{-1}).

As has been done previously,[63,79] the electronic structures of the **1-X** series were analyzed using classic LFT, specifically with the angular overlap model (AOM). This LFT/AOM analysis only employs a d^7 basis; thus, it does not take into account the possibility of ligand "non-innocence". Such an effect may be operative for **1-I**, as previously seen in a Mn(III) diiodido complex.[80] Except for **1-Cl**, the **1-X** complexes do not exhibit crystallographic threefold symmetry; however, DFT geometry optimizations (*vide infra*) suggest that structures in solution may be closer to trigonally symmetric due to the absence of lattice constraints. For the relatively simple LFT analysis used here, ideal C_{3v} symmetry was imposed by use of average X−Co−N_{Tp} bond angles (see Table 6) and $\phi \equiv 0$, 120, and 240°

https://doi.org/10.1021/acs.inorgchem.2c04468
Inorg. Chem. 2023, 62, 5984−6002

Table 6. Visible−NIR Electronic Absorption Data for 1-X Series of Co(II) Complexes (All Values in cm^{-1}) and Transition Energies Computed by QCT, AOM/LFT, and AILFT

complex		$^4A_2 \rightarrow {}^4E\ (T_1,F)$	$^4A_2 \rightarrow {}^4A_2\ (T_1,F)$	$^4A_2 \rightarrow {}^4A_2\ (T_1,P)$	$^4A_2 \rightarrow {}^4E\ (T_1,P)$
1-F	Exper.	6710	11,600	15,180	17,390, 18,180
	Calcd (AOM)[a,b]	6710	11,600	15,180	17,785
	Calcd (AILFT)[b,c]	6180	10,156	15,285	17,645
	Calcd (QCT)[d]	6995, 7265	12,067	18,293	20,847, 20,936
1-Cl	Exper.	6040	10,480	16,670	15,150, 15,670
	Calcd (AOM)[a,b]	6040	10,480	15,150	16,170
	Calcd (AILFT)[b,c]	5451	9293	16,034	16,046
	Calcd (QCT)[d]	6030, 6395	10,952	19,371	18,864, 19,093
1-Br	Exper.	5810	10,130	16,610	15,340, 15,770
	Calcd (AOM)[a,b]	5810	10,130	15,340	16,190
	Calcd (AILFT)[b,c]	5222	9112	16,348	15,828
	Calcd (QCT)[d]	5856, 6272	10,705	19,525	18,763, 18,810
1-I	Exper.	5670	9700	16,500	14,690, 15,360
	Calcd (AOM)[a,b]	5670	9700	14,690	15,930
	Calcd (AILFT)[b,c]	4928	8720	16,356	15,189
	Calcd (QCT)[d]	5532, 5917	10,210	19,657	18,373, 18,468

[a]These calculations employed average ∠X-Co-N_{Tp} values: **1-F** = 122.04°; **1-Cl** = 124.42° (crystallographically threefold symmetric); **1-Br** = 121.22°; **1-I** = 121.01°. [b]The AOM parameters are provided in Table S3. [c]These entries employed values of AOM bonding parameters that had been calculated by an anonymous reviewer using AILFT and provided to us in the review process. We then performed fits with the AOM parameters fixed at these values but allowed the Racah *B* value to vary, as *B* was not provided by the reviewer. [d]QCT calculations employed DFT geometry-optimized structures.

for the three N_{Tp} donors. Correspondingly, the donor properties of the three N_{Tp} ligands were held to be equivalent. Although Plugis *et al.* included asymmetric π-donation by the N_{Tp} ligands (*i.e.*, $\varepsilon_{\pi-s} \neq 0$),[79] we found this interaction to be unnecessary for the present level of analysis. For the halido ligands, symmetric (cylindrical) π-donation was included (*i.e.*, $\varepsilon_{\pi-s} = \varepsilon_{\pi-c} \neq 0$). The observed bands were fitted in the absence of SOC, and the doublet states were disregarded (the Racah *C* parameter was set at a very high value).

As shown in Table 6, the AOM-LFT approach provides excellent fits for the observed bands in the NIR region. However, for bands in the visible region, it was impossible to obtain successful fits unless the $^4A_2 \rightarrow {}^4E(T_1,P)$ transitions occur at a higher energy than the $^4A_2 \rightarrow {}^4A_2(T_1,P)$ transition (as indeed found for **1-F**). Previous LFT studies of $[CoCl(Tp^{R1,R2})]$ complexes[63,79] provided the same energy ordering, yet these studies lacked complexes analogous to **1-Br** and **1-I**. Given that the overall splitting within the parent $^4A_2(F) \rightarrow {}^4T_1(P)$ band is relatively small for all but **1-F**, this discrepancy does not negate the usefulness of the AOM parameters obtained for the entire **1-X** series (Table S3). The four complexes provide similar Racah *B* parameters: $B = 725 \pm 10\ cm^{-1}$ (~73% of the free-ion value[81]), consistent with previously studied $[CoCl(Tp^{R1,R2})]$ complexes ($B_{avg} = 743\ cm^{-1}$).[63,79] In agreement with the previous work, the N_{Tp} donors all had ε_σ in the range 3400−4000 cm^{-1}, with ε_σ increasing in the direction **1-I** < **1-Br** < **1-Cl** < **1-F**. This trend is expected based on the greater ionic character of bonding for the smaller halides. Concerning the halide ligand itself, the trend is less clear. The fluoride ligand is by far the strongest σ-donor ($e_\sigma(F) = 3968.0\ cm^{-1}$). The ε_σ values for the other three halides fall in the range $\varepsilon_\sigma = 2260 \pm 200\ cm^{-1}$, with the iodide ligand being the strongest donor (the most covalent of the three). Likewise, the fluoride ligand is the strongest π-donor [$\varepsilon_\pi(F) = 1764\ cm^{-1}$], with the other three halides in the range $\varepsilon_\pi = 430 \pm 130\ cm^{-1}$.

The above discussion involved only the quartet states of **1-X**. The level of LFT employed here did not warrant attempting to fit the data using spin doublet states and SOC. However, if $C = 4.3B$ (*i.e.*, the free-ion ratio[81]) is assumed for **1-Cl**, then a doublet excited state, $^2E(^2E,G)$, is predicted at ~15,400 cm^{-1}, close to the $^4A_2(F) \rightarrow {}^4T_1(P)$ band. More relevantly, the shoulder seen above the $^4A_2(F) \rightarrow {}^4T_1(P)$ band (at ~18,000 cm^{-1} for **1-Cl**, **1-Br**, and **1-I**) may be due to nominally spin-forbidden (but dipole-allowed) transitions to $^2A_2(^2T_1,H,P)$ and $^2E(^2T_1,H,P)$. These spin-forbidden transitions were previously noted by Plugis *et al.* but not specifically assigned.

An expert reviewer provided an alternate set of AOM parameters for the **1-X** series that were calculated not by fitting the observed bands, but entirely by theory using the *ab initio* LFT (AILFT) method developed by Atanasov and co-workers.[82,83] The band energies arising from these parameters are labeled AILFT in Table 6, and the complete set of AOM parameters are provided in Table S3. In the case of **1-F**, the AILFT-derived parameters and energies are qualitatively the same as those generated by our fitting of the observed vis−NIR bands described above. Both methods characterize the fluoride ligand as a strong σ- and π-donor and yield similar parameters for the N_{Tp} donors. The consequence is that, in both models, the $^4A_2 \rightarrow {}^4E(T_1,P)$ transition is calculated at a higher energy than the $^4A_2 \rightarrow {}^4A_2\ (T_1,P)$ transition. The situation for the other three **1-X** complexes is quite different. For **1-Cl**, AILFT-derived parameters provided very similar energies for the two transitions within $^4T_1(P)$. In the cases of **1-Br** and **1-I**, the $^4A_2 \rightarrow {}^4E(T_1,P)$ transition is indeed calculated at a lower energy than the $^4A_2 \rightarrow {}^4A_2(T_1,P)$ transition−consistent with experiment and the opposite of what the AOM fits required (*vide supra*). This result is the consequence of $\varepsilon_\sigma(X)$ (X = Cl, Br, and I) being relatively low and $\varepsilon_\pi(X)$ being large and negative for X = Cl, Br, and I in the AILFT model (Table S3). These $\varepsilon_\pi(X)$ values unintuitively imply that the heavier halide ligands act as π-acceptors. We also conducted AOM fits in which the AILFT values were used as starting points and parameters were

https://doi.org/10.1021/acs.inorgchem.2c04468
Inorg. Chem. 2023, 62, 5984−6002

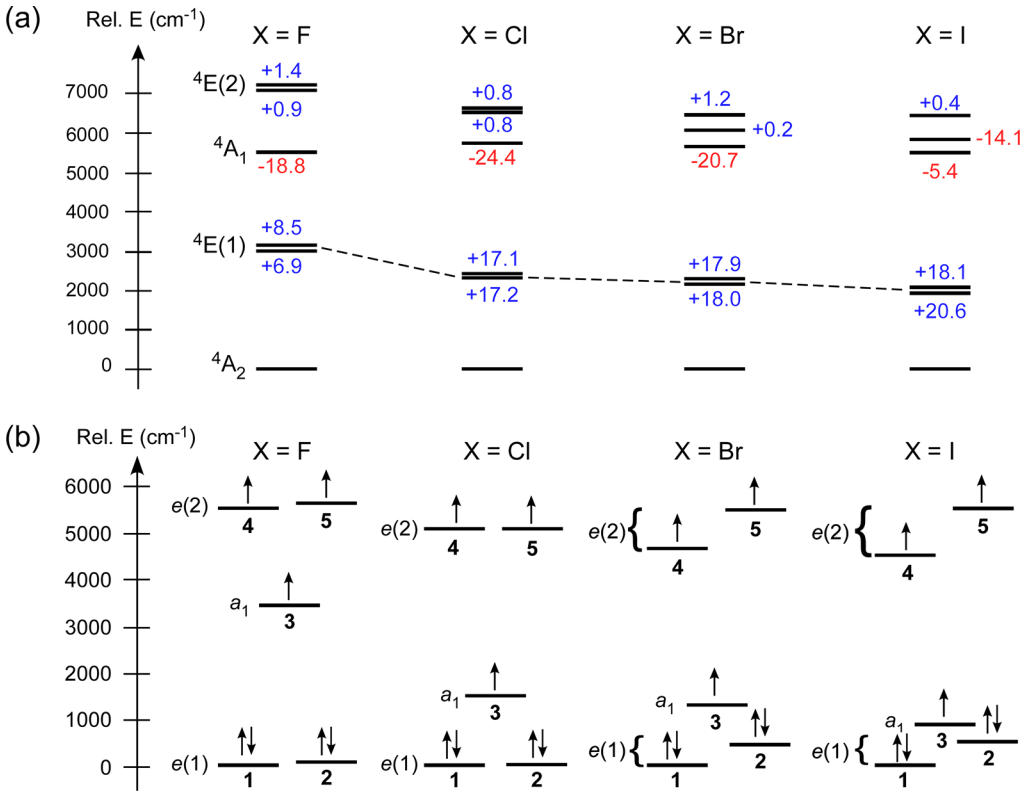

Figure 9. (a) Energies of the six lowest-energy quartet states obtained from CASSCF/NEVPT2 calculations of **1-X** complexes. Calculations employed the crystallographic structures. The blue and red numbers represent the positive and negative contributions, respectively, of each excited state to the *D*-value. (b) Energy-level diagram for the Co 3d orbitals of **1-X** complexes derived from AILFT treatment of NEVPT2 transition energies. The plots of **1-Br** and **1-I** in both (a,b) are averages of the two crystallographic isomers (A and B).

allowed to vary within relatively narrow ranges so as to maintain correspondence with the starting values. However, this approach resulted in unrealistic $\varepsilon_\sigma(X)$ and $\varepsilon_\pi(X)$ values for X = Cl, Br, and I (Table S3).

The visible−NIR absorption spectra of the five-coordinate complexes (**2-X**) in CH_2Cl_2 solution are quite similar to those measured for the **1-X** congeners. The most notable difference is a modest blue shift in the $^4A_2 \rightarrow {}^4A_2(F)$ transition by 500−900 cm^{-1} (Figure S9). Given the spectral similarities between the **1-X** and **2-X** series, it is not clear whether the latter set of complexes maintains a five-coordinate geometry in solution. Instead, the less constrained environment in solution may lead to full or partial dissociation of a pyrazole donor to relieve steric crowding. This conclusion is supported by literature precedents,[84] as well as the fact that **2-X** solutions change from purple to blue over time.

Electronic Structure Calculations. The relationship between molecular structure and magnetic anisotropy was further probed using QCT. These *ab initio* calculations utilized the complete active space self-consistent field (CASSCF) approach, in which the CAS(7,5) active space consisted of seven electrons distributed across the five Co 3d orbitals. The effect of dynamic correlation on the energies of ligand-field states was accounted for using second-order *N*-electron valence perturbation theory (NEVPT2). Spin−Hamiltonian parameters (*g*-values, *D*, and |*E*/*D*|) computed for the **1-X** series are provided in Table 4. QCT correctly predicts the unique ZFS parameters of **1-F**, namely, its rhombic **D**-tensor and smaller magnitude of *D* (relative to other members of the series). Similarly, the computed *g*-values and ZFS parameters of **1-Cl** are in excellent agreement with the experiment. QCT predicts a modest increase in the *D*-value with the size of the halide ligand, from +11.0 cm^{-1} (**1-Cl**) to +19.8 cm^{-1} (B isomer of **1-I**). This trend contradicts our experimental finding that the *D*-values of **1-Cl**, **1-Br**, and **1-I** are similar in magnitude and uncorrelated with halide size. Nevertheless, the QCT calculations reproduce the increase in rhombicity (Cl < Br < I) observed by HFEPR.

Significantly, the QCT results allow us to rationalize the observed ZFS parameters for the **1-X** series. The ZFS of the *S* = 3/2 ground state is largely due to second-order SOC-induced mixing between the $^4A_2$ ground state and low-lying quartet excited states. The dominant contribution arises from the parent $^4T_2(F)$ excited state in T_d symmetry, which splits into the $^4A_1$ and ^4E terms in C_{3v} symmetry. The QCT calculations indicate that the lower-energy ^4E state makes a positive contribution to the *D*-value, whereas the higher-energy $^4A_1$ state makes a negative contribution. Thus, as described in previous studies of similar Co(II) complexes,[22,83] the sign and magnitude of the *D*-values are determined by the relative energies of the $^4A_1$ and ^4E states, whereas rhombicity (*E*/*D*) arises from splitting of the ^4E state. As illustrated in Figure 9a, the ^4E state of **1-F** is higher in energy than its counterparts in the other **1-X** complexes by an average of 920 cm^{-1}. In contrast, the energy of the $^4A_1$ state is relatively constant at 5650 ± 100 cm^{-1} across the series. The destabilization of the ^4E state of **1-F** diminishes its positive contribution to the **D**-tensor by nearly half, thereby reducing the magnitude of ZFS (Figure 9a). In contrast, the larger $^4A_1/{}^4E$ splitting of **1-Cl**, **1-Br**, and **1-I** accounts for their positive and larger *D*-values.

https://doi.org/10.1021/acs.inorgchem.2c04468
Inorg. Chem. 2023, 62, 5984−6002

The shifts in state energies across the **1-X** series are due to changes in the relative energies of the Co 3d orbitals, as illustrated in Figure 9b. These orbital energies are derived from analysis of the NEVPT2 transition energies using *ab initio* LFT (AIFLT), as developed by Atanasov and co-workers.[13,85] In C_{3v} symmetry, there are two degenerate pairs of 3d orbitals with *e* symmetry that possess mixed d_{xz}/d_{yz} and $d_{xy}/d_{x^2-y^2}$ character. The 3d orbital with a_1 symmetry (d_{z^2}) is pointed along the axial Co−X bond axis. Two trends are evident in Figure 9b. First, the energy of the Co d_{z^2} orbital decreases with increasing halide size, with a particularly dramatic drop from **1-F** to **1-Cl**. The relative energy of this a_1 orbital correlates with the energy of the low-energy $^4A_2 \rightarrow {}^4E(1)$ transition, as the latter involves promotion of 3d electrons from the fully occupied $e(1)$ pair to the singly occupied a_1 orbital. Therefore, the very strong σ-donor ability of the fluoro ligand, as confirmed by our AOM-LFT analysis, is responsible for the unique ZFS parameters of **1-F** within the **1-X** series. Second, the increase in rhombicity with halide size is clearly manifest in the computed splitting of the *e* pairs of orbitals. The orbitals are essentially degenerate for **1-Cl**, but the gap widens to ∼500 cm^{-1} for the $e(1)$ orbitals of **1-I** due to structural distortions that are evident in the XRD data.

To better understand the relationship between ZFS and structural distortions, we also conducted QCT calculations using alternative models of **1-F**, **1-Br**, and **1-I** with imposed trigonal symmetry (recall that **1-Cl** already possesses crystallographic C_3 symmetry). The resulting ZFS parameters are provided in Table S4. As expected, the computed rhombicities (E/D) of the symmetrized models are much smaller than the experimental values. The magnitude of the computed *D*-values correlates with the size of the halide ligand and increases across the series: $|D|$ = 2.8 (F), 11.0 (Cl), 14.7 (Br), and 18.1 (I). Although this trend is not evident in the experimental data, the halide effect predicted computationally for the C_3 models is due to the fact that the σ- and π-donor strengths of the halides diminish with size—a trend consistent with parameters derived from AOM and AILFT treatments of the absorption data (see above). The weaker ligand field of the larger halides lowers the relative energy of the $^4E(1)$ excited state, thereby increasing its positive contribution to the **D**-tensor.

Starting from the C_3-symmetric models, gas-phase geometry optimizations of the **1-X** series were performed to gauge the relative impact of external and intrinsic factors on molecular geometry. Metric parameters of the crystallographic and computational structures are compared in Table S5. The optimized structures exhibit only modest variations in X1−Co1−N_{Tp} bond angles, which fall in a narrow range of 120.5−122.9°. Thus, the geometric distortions away from C_3 symmetry that are so pronounced in the X-ray structures of **1-Br** and **1-I** are likely due to extrinsic lattice effects, validating the use of trigonal symmetry in the LFT-AOM model to analyze solution electronic absorption spectra (*vide supra*). Not surprisingly, the XRD structures provide the best agreement between the computed and experimental (*i.e.*, solid state) E/D ratios, whereas the magnitude of *D* is less sensitive to deviations from C_3 symmetry (Table S4).

The QCT calculations also provided ligand-field transition energies and simulated absorption spectra, which are shown in Table 6 and Figure S10, respectively. These results were obtained with geometry-optimized models of **1-X** that better account for the solution-state structures. The CASSCF/NEVPT2 approach tends to overestimate the energies of LF transitions; nevertheless, general trends in band energies across the **1-X** series are well reproduced. Notably, the relative energies of the computed $^4A_2 \rightarrow {}^4E(T_1,P)$ and $^4A_2 \rightarrow {}^4A_2(T_1,P)$ transitions match the experimental order for each complex, unlike the AOM fitting results described above. The good agreement between experimental and computational parameters validates the electronic-structure descriptions provided by the CASSCF/NEVPT2 approach.

The QCT computational methodology was also applied to the **2-X** series, and the results are summarized in Table 5. QCT accurately reproduces the large and negative anisotropies of the **2-X** complexes as well as the relative magnitude of the *D*-values (**2-Cl** < **2-Br** < **2-I**). The computed E/D-values are also in excellent agreement with the experiment, although the anisotropy of the **g**-tensors is overestimated. The orientations of the **D**-tensors are depicted in Figure S11. The dominant contributor to the easy-axis anisotropy is a low-energy excited state that lies only 640 cm^{-1} (**2-Cl**), 460 cm^{-1} (**2-Br**), or 420 cm^{-1} (**2-I**) above the ground state. As described in our previous study of five-coordinate Co(II) complexes,[54] structural distortions enforced by the Tp framework shrink the energy gap between the highest-energy doubly-occupied Co 3d orbital and the lowest-energy singly occupied 3d orbital, as shown in Figure 10 for **2-Cl**. Because the latter orbital is oriented along the Co−X axis, the elongation of this bond diminishes the energy of the lowest-energy excited state, resulting in more negative *D*-values as the halide size increases. Significantly, for both the **1-X** and **2-X** series, the computational results indicate that the observed shifts in *D*-values are caused entirely by structural changes that perturb Co 3d orbital energies, not heavy-atom effects. In support of this conclusion, the effective SOC constants (ζ) provided by AILFT are essentially the same for each complex, falling between ζ = 500−515 cm^{-1}.

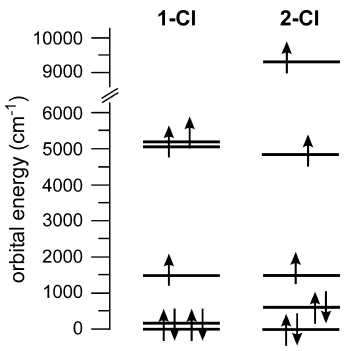

Figure 10. Energy-level diagrams for the Co 3d orbitals of **1-Cl** and **2-Cl** complexes derived from AILFT treatment of NEVPT2 transition energies. Calculations employed the crystallographic structures.

DISCUSSION

This study has examined the impact of donor-atom size and coordination number on the structural, magnetic, and electronic properties of high-spin cobalt (II)−halide complexes supported by substituted Tp ligands. Two related sets of complexes were prepared and characterized with X-ray crystallography. The four-coordinate series, [CoX($Tp^{tBu,Me}$)] (**1-X**; X = F, Cl, Br, and I), exhibit actual or distorted C_3 symmetry with the halide ligand positioned along the axis of rotation. Analogous complexes with the less sterically

https://doi.org/10.1021/acs.inorgchem.2c04468
Inorg. Chem. 2023, 62, 5984−6002

demanding $Tp^{Ph,Me}$ scaffold are capable of binding a monodentate pyrazole ligand, giving rise to the five-coordinate series $[CoX(Tp^{Ph,Me})(Hpz^{Ph,Me})]$ (**2-X**; X = Cl, Br, and I) that possess distorted trigonal-bipyramidal geometries. The spin-Hamiltonian parameters of each complex were measured by dc magnetic susceptibility, HFEPR spectroscopy, and FIRMS. Remarkable agreement was observed among the three techniques, especially with regards to the ZFS values (D and E). The relationship between the molecular structure, ligand-field energies, and ZFS was further elucidated using *ab initio* CASSCF/NEVPT2 and AOM-LFT calculations. The computational results have allowed us to rationalize the observed ZFS parameters for the **1-X** and **2-X** series.

Despite the increase in halide size, only minor variations are observed in the experimental spin-Hamiltonian parameters of **1-Cl**, **1-Br**, and **1-I**. Each complex exhibits a positive D-value of 11−13 cm^{-1} and g_{ave} of 2.33 ± 0.02 (Table 4). The most notable trend is an increase in rhombicity (E) in the order Cl < Br < I, which is also apparent in the splitting of the parent $^4A_2 \rightarrow {}^4T_1(P)$ transition in the visible region of the absorption spectra (Figure 8). *Ab initio* LFT (AILFT) calculations indicate that the effective SOC parameter (ζ_{eff}) is not affected by halide size, thus the modest changes in ZFS parameters among **1-Cl**, **1-Br**, and **1-I** are attributed to ligand-field perturbations. The lack of a pronounced "heavy-atom effect" in the **1-X** series is likely due to the ionic nature of the Co−X bonds, which limits the amount of halide character in the Co 3d-based MOs. Thus, the mechanism for increasing ZFS *via* cobalt-halide covalency is not operative in the **1-X** series.

The unique member of the **1-X** series is the fluoride complex (**1-F**), which exhibits a much smaller D-value ($|D|$ = 3.9 cm^{-1}) and an E/D ratio at the rhombic limit (Table 4). Our *ab initio* calculations indicate that the decrease in ZFS arises from the destabilization of the low-lying ^4E state, which is the dominant positive contributor to the **D**-tensor (Figure 9). This destabilization is the result of the short Co−F bond distance and much stronger σ-donating ability of the fluoride ligand (relative to Cl, Br, and I), which increase the relative energy of the Co $3d_{z^2}$ orbital. From these results, it is clear that the donor properties of the fluoride ligand diverge greatly from those of the Cl/Br/I set. Thus, there is a clear "fluoro effect", as substitution of the heavier halides with F causes a dramatic change in ligand-field energies and hence ZFS parameters. It is likely that this "fluoro effect" can be generalized to other transition-metal complexes, although its precise impact on the sign and magnitude of D is difficult to predict.

Magnetic susceptibility and HFEPR experiments determined that the five-coordinate **2-X** complexes exhibit large and negative D-values. The observation of zero-field transitions by FIRMS yielded ZFS parameters consistent with QCT calculations. The sizable anisotropy of the **2-X** series arises from SOC-induced mixing between the ground state and a single low-lying excited state. There is an apparent heavy-atom effect, as the magnitude of D increases with halide size (Table 5). However, our *ab initio* calculations suggest that these changes arise from elongation of the Co−X bond, which lowers the energy of the first excited state through stabilization of the lowest-energy singly occupied Co 3d orbital (Figure 10). The large, negative D-values of the **2-X** series suggest that these complexes may function as single-molecule magnets—a possibility that will be explored in future studies.

CONCLUSIONS

Based on the results of this systematic study, we are now in a position to answer the question posed in the title: is there a halide effect on magnetic anisotropy? The answer is both "yes" and "no". On the one hand, our results failed to find evidence that heavy halide ligands with much larger free-atom SOC constants enhance ZFS through metal−ligand covalency. On the other hand, changes in the halide ligand are indeed capable of modulating ZFS, but these shifts are the result of ligand-field effects. Specifically, the heavier halides are weaker and softer ligands, and thus the increase in the magnitude of D is often due to the stabilization of low-lying ligand-field excited states, which enhance mixing *via* SOC. Indeed, the dramatic differences in ZFS parameters between the **1-X** and **2-X** series indicate that coordination number and geometry are the dominant factors in shaping the magnetic properties of Co(II) complexes. Substantial cobalt-ligand covalency may be possible only with more electropositive donors, such as the Ge- and Sn-based ligands employed by Freedman.[22] While the implications of our results for other transition-metal ions remain to be seen, it is clear that the heavy-atom effect is not a general phenomenon for modulating ZFS. This conclusion is consistent with previous studies[25,36,37] which found that the impact (or lack thereof) of halide substitutions on ZFS depends on the complex interplay of multiple factors. Thus, the particular composition and structure of each system must be taken into account before attributing trends in D-values to heavy-atom or halide effects.

EXPERIMENTAL AND COMPUTATIONAL METHODS

Materials. Solvents and reagents were purchased from commercial sources and used as received, unless otherwise noted. Some solvents (CH_2Cl_2, CH_3CN, THF, and Et_2O) were purified by drying over CaH_2 or NaH, followed by distillation. After degassing *via* multiple freeze-pump-thaw cycles, the solvents were stored in the glovebox over activated molecular sieves. The Co(II) complexes were synthesized and handled under an inert atmosphere using a Vacuum Atmospheres Omni-Lab glovebox. The following compounds were prepared using published procedures: 5-methyl-3-phenylpyrazole ($Hpz^{Ph,Me}$),[86] $K(Tp^{tBu,Me})$,[87] $K(Tp^{Ph,Me})$,[86] and $[CoCl(Tp^{Ph,Me})]$.[62] Sample purity was evaluated using elemental analysis data collected at Midwest Microlab, LLC, in Indianapolis, IN.

General Procedure for Syntheses of $[Co^{II}X(Tp^{tBu,Me})]$ (1-X; X = Cl, Br, and I). THF solutions of $K(Tp^{tBu,Me})$ (287 mg, 0.62 mmol, 1 equiv) and CoX_2 (0.68 mmol, 1.1 equiv) were combined at room temperature. The resulting blue solutions were stirred for 2 h, followed by filtration through Celite to remove the white precipitate. For **1-Cl**, the volume of the solution was reduced substantially, and pentane was added. Blue prismatic crystals appeared during the slow evaporation of the solvent. For **1-Br** and **1-I**, the solvent was fully evaporated after filtration, and the resulting blue solid was taken up in a CH_2Cl_2/pentane mixture. Slow evaporation yielded crystals suitable for crystallographic analysis. In each case, the crystals were collected and dried under vacuum to provide analytically pure material for magnetometry and spectroscopic studies.

$[CoCl(Tp^{tBu,Me})]$ (1-Cl). Yield = 229 mg (71%). ^1H NMR (300 MHz, $CDCl_3$): δ = 78.6 (s, 3H, 4-*H*-pz), 13.2 (s, 9H, 5-Tp-CH_3), 8.9 (s, 27H, $-C(CH_3)_3$), −19.3 ppm (br s, 1H, B*H*). UV−vis [λ_{max}, nm (ε, M^{-1} cm^{-1}) in CH_2Cl_2]: 1655 (60), 954 (60), 638 (521). FTIR (cm^{-1}, solid): 2952, 2565 [ν(BH)], 1537, 1470, 1429, 1381. Anal. Calcd for $C_{24}H_{40}BClCoN_6$: C, 55.67; H, 7.79; N, 16.23. Found: C, 55.82; H, 7.61; N, 15.93.

$[CoBr(Tp^{tBu,Me})]$ (1-Br). Yield = 244 mg (70%). ^1H NMR (400 MHz, $CDCl_3$): δ = 78.4 (s, 3H, 4-*H*-pz), 14.3 (s, 9H, 5-Tp-CH_3), 9.2 (s, 27H, $-C(CH_3)_3$), −18.4 ppm (br s, 1H, B−*H*). UV−vis [λ_{max}, nm

https://doi.org/10.1021/acs.inorgchem.2c04468
Inorg. Chem. 2023, 62, 5984−6002

(ε, M^{-1} cm^{-1}) in CH_2Cl_2]: 1721 (70), 987 (110), 634 (700), 602 (480). FTIR (cm^{-1}, solid): 2960, 2572 [ν(BH)], 1537, 1472, 1421, 1381. Anal. Calcd for $C_{24}H_{40}BBrCoN_6$: C, 51.27; H, 7.17; N, 14.95. Found: C, 50.99; H, 7.09; N 14.69.

[CoI($Tp^{tBu,Me}$)] (1-I). Yield = 276 mg (73%). ^1H NMR (400 MHz, $CDCl_3$): δ = 77.2 (s, 3H, 4-*H*-pz), 16.2 (s, 9H, 5-Tp-CH_3), 8.9 (s, 27H, −C(CH_3)$_3$), −14.6 ppm (br s, 1H, B−*H*). UV−vis [λ_{max}, nm (ε, M^{-1} cm^{-1}) in CH_2Cl_2]: 1763 (80), 1030 (170), 681 (670), 651 (760) 606 (660). FTIR (cm^{-1}, solid): 2956, 2557 [ν(BH)], 1543, 1473, 1421, 1382. Anal. Calcd for $C_{24}H_{40}BICoN_6$: C, 47.31; H, 6.62; N, 13.79. Found: C, 47.56; H, 6.90; N, 13.46.

[CoF($Tp^{tBu,Me}$)] (1-F). To a solution of **1-Cl** (123 mg, 0.24 mmol, 1.0 equiv) in toluene (10 mL) was added thallium fluoride (139 mg, 0.59 mmol, 2.5 equiv). Warning: Thallium salts are toxic and should be handled with extreme caution. The solution was stirred overnight and then filtered. After the removal of the solvent, the solid was washed with diethyl ether and dried. The remaining residue was taken up in CH_2Cl_2. Violet crystals were grown *via* slow evaporation from a CH_2Cl_2/pentane solution. Yield = 112 mg (94%). ^1H NMR (400 MHz, $CDCl_3$): δ = 75.7 (s, 3H, 4-*H*-pz), 13.3 (s, 9H, 5-Tp-CH_3), 3.1 ppm (s, 27H, −C(CH_3)$_3$). UV−vis [λ_{max}, nm (ε, M^{-1} cm^{-1}) in CH_2Cl_2]: 1480 (120), 862 (20), 658 (640), 575 (450), 550 (350). FTIR (cm^{-1}, solid): 2955, 2546 [ν(BH)], 1539, 1465, 1424, 1384. Anal. Calcd for $C_{24}H_{40}BFCoN_6$: C, 57.50; H, 8.04; N, 16.76. Found: C, 57.64; H, 7.95; N, 16.45.

[CoBr($Tp^{Ph,Me}$)]. A round-bottom flask equipped with a magnetic stir bar was charged with $CoBr_2$ (243 mg, 1.11 mmol, 1 equiv) and MeOH (1 mL). A solution of K(Tp^{PhMe}) (580 mg, 1.11 mmol, 1 equiv) in CH_2Cl_2 was added dropwise, and the resulting dark blue mixture was stirred for 2 h. The solvent was evaporated under vacuum, and the solid was taken up in CH_2Cl_2. After filtration through Celite, the solvent was removed to give a residue that was washed with Et_2O and dried under vacuum. The crude material was used without further purification. Yield = 610 mg (88%). ^1H NMR (300 MHz, $CDCl_3$): δ = 75.9 (s, 3H, 4-*H*-pz), 17.3 (s, 6H, Ph-Tp-*H*), 13.9 (s, 9H, Tp-CH_3), 8.6 (s, 6H, Ph-Tp-*H*), 7.9 (s, 3H, Ph-Tp-*H*), −25.4 ppm (br s, 1H, B−*H*).

[CoI($Tp^{Ph,Me}$)]. The method of preparation was the same as the one described above for [CoBr($Tp^{Ph,Me}$)], except that CoI_2 (344 mg, 1.1 mmol, 1 equiv) was used instead of $CoBr_2$. Yield = 611 mg (83%). ^1H NMR (400 MHz, $CDCl_3$): δ = 75.7 (s, 3H, 4-*H*-pz), 16.9 (s, 6H, Ph-Tp-*H*), 13.0 (s, 9H, Tp-CH_3), 8.2 (s, 6H, Ph-Tp-*H*), −22.4 ppm (br s, 1H, B−*H*).

[CoCl($Tp^{Ph,Me}$)($Hpz^{Ph,Me}$)] (2-Cl). A small amount of Et_3N (~40 μL) was added to a 1:1 CH_2Cl_2:MeOH solution of $Hpz^{Ph,Me}$ (54 mg, 0.34 mmol, 1 equiv) and [CoCl($Tp^{Ph,Me}$)] (195 mg, 0.34 mmol, 1 equiv). The resultant mixture was stirred for 1 h to give a purple-colored solution. After removal of the solvent under vacuum, the residue was taken up in CH_2Cl_2 and filtered. The volume of solvent was reduced and layered with excess pentane to provide a pure compound. Yield = 163 mg (65%). X-ray quality crystals were obtained by vapor diffusion of pentane into a concentrated benzene solution. FTIR (cm^{-1}, solid): 3254 [ν(NH)], 2538 [ν(BH)]. Anal. Calcd for $C_{40}H_{38}BClCoN_8$: C, 65.28; H, 5.20; N, 15.23. Found: C, 65.01; H, 5.06; N, 14.99.

[CoBr($Tp^{Ph,Me}$)($Hpz^{Ph,Me}$)] (2-Br). [CoBr($Tp^{Ph,Me}$)] (610 mg, 0.98 mmol, 1 equiv) and $Hpz^{Ph,Me}$ (155 mg, 0.98 mmol, 1 equiv) were dissolved in CH_3OH (100 mL) and stirred until all the solids were dissolved, yielding a purple solution. After 1 hour, the solvent was removed under vacuum. The resulting solid was dissolved in CH_2Cl_2 and filtered. The solution was reduced in volume and then layered with pentane to provide a recrystallized solid. Yield = 491 mg (64%). X-ray quality crystals were obtained by vapor diffusion of pentane into a concentrated benzene solution of the complex. FTIR (cm^{-1}, solid): 3235 [ν(NH)], 2536 [ν(BH)]. Anal. Calcd for $C_{40}H_{38}BBrCoN_8$: C, 61.56; H, 4.91; N, 14.36. Found: C, 61.52; H, 4.62; N, 14.62.

[CoI($Tp^{Ph,Me}$)($Hpz^{Ph,Me}$)] (2-I). In a scintillation vial equipped with a magnetic stir bar, [CoI($Tp^{Ph,Me}$)] (509 mg, 0.76 mmol, 1 equiv) and $Hpz^{Ph,Me}$ (120 mg, 0.76 mmol, 1 equiv) were dissolved in CH_3OH and stirred until all the solids were dissolved. The purple mixture was stirred for an hour, followed by the removal of the solvent under vacuum. The solid was dissolved in CH_2Cl_2, filtered, and then layered with pentane. The mixture provided violet crystals that were crushed into a fine powder and washed twice with ether. Yield = 444 mg (71%). X-ray quality crystals were obtained by vapor diffusion of pentane into a concentrated benzene solution. FTIR (cm^{-1}, solid): 3236 [ν(NH)], 2530 [ν(BH)]. Anal. Calcd for $C_{40}H_{38}BICoN_8$: C, 58.06; H, 4.63; N, 13.54. Found: C, 58.26; H, 5.18; N, 12.93.

X-ray Crystallography. X-ray diffraction experiments using single crystals of the **1-X** and **2-X** complexes were conducted at 100 K with an Oxford Diffraction (Rigaku Corporation) SuperNova diffractometer. The instrument consists of dual-wave micro-focus sealed-tube sources (Cu and Mo K_α), X-ray mirror optics, an Atlas CCD detector, and an open-flow Cryojet LN_2 cooling device (Oxford Instruments). An absorption correction based on the real shape of the crystals was applied, followed by a polynomial empirical procedure within the CrysAlis Pro (Rigaku, 2018) program package. The structures were solved using charge-flipping[88] and intrinsic phasing methods, then refined utilizing an anisotropic approximation for non-hydrogen atoms in a least-squares procedure.[89] Hydrogen atoms were positioned geometrically, and a riding/rotating model was applied during refinement. The experimental parameters are summarized in Tables S1 and S2. The structure of **1-Br** is disordered; however, the population of the second component is just 6.6%. Therefore, it was only possible to locate the positions of the Co and Br atoms of the second component. The structures of **1-Br** and **1-I** are isomorphic with the previously reported structure of [NiI($Tp^{tBu,Me}$)].[90] Crystallographic data (CIF format) for the X-ray structures of the **1-X** and **2-X** series can be accessed from the Cambridge Crystallographic Data Centre (CCDC) under the deposition numbers 2226822−2226826 and 2244005−2244006.

Magnetic Susceptibility Measurements. Variable-temperature DC susceptibility data and VHVT (variable field fixed temperature) magnetization data for **1-Cl**, **1-Br**, **1-I**, and **2-X** complexes were measured with a MPMS 3 Quantum Design SQUID magnetometer at the University of Wisconsin−Madison. Variable-temperature DC susceptibility data and VTVH (variable temperature fixed field) magnetization data for complex **1-F** were measured with a MPMS 3 Quantum Design SQUID magnetometer at the Max Planck Institute for Chemical Energy Conversion (MPI-CEC) in the Joint Workspace of the Max-Planck-Institut für Kohlenforschung (MPI-KoFo). Susceptibility data were obtained by cooling to ~2 K in the absence of a magnetic field and subsequently measuring the magnetic moment from the starting temperatures to 300 K in an applied 1000 G DC magnetic field. A deviation in the trend of the data was visible in a few datapoints for **1-F** from 39 to 53 K due to an impurity; these datapoints were thus excluded from modeling. An unusual bump was also visible in the **1-Cl** data near 10 K, which is likely due to the partial (but minor) orientation of the microcrystalline sample. Thus, data below 15 K were excluded from modeling. VHVT data were collected for the **1-X** and **2-X** complexes (X = Cl, Br, and I) at temperatures of 2, 4, 6, and 8 K as the field strength was increased from 0 to 7 T. The 2 K VHVT measurement for the **2-Br** complex was deemed unreliable due to a discontinuity in the data and was thus excluded from the fit. VTVH data were collected for **1-F** at fields of 1, 4, and 7 T as the temperature was increased from 2 to 300 K. Experimental susceptibility data were corrected for underlying diamagnetism using Pascal's constants.[91] The susceptibility and magnetization data for the **1-X** and **2-X** complexes (X = Cl, Br, and I) were modeled simultaneously using the fitting program PHI.[92] The susceptibility and magnetization data for **1-F** were modeled simultaneously using JulX20.[93] All data were parameterized using the following spin Hamiltonian

$$\hat{\mathcal{H}} = \beta\hat{S}\cdot\boldsymbol{g}\cdot\vec{B} + \hat{S}\cdot\boldsymbol{D}\cdot\hat{S} = \beta\hat{S}\cdot\boldsymbol{g}\cdot\vec{B} + D\left(\hat{S}_z^{\,2} - \frac{1}{3}S(S+1)\right) + E(\hat{S}_x^{\,2} - \hat{S}_y^{\,2})$$

https://doi.org/10.1021/acs.inorgchem.2c04468
Inorg. Chem. 2023, 62, 5984−6002

where β is the Bohr magneton, $\vec{H}$ is the applied external magnetic field, and $\vec{S}$, $\boldsymbol{g}$, and $\boldsymbol{D}$ are the spin vector, electron **g**-tensor, and zero-field splitting (ZFS) tensors, respectively. All compounds were modeled with axial $\boldsymbol{g}$ ($g_z = g_\parallel$; $g_x = g_y = g_\perp$) and $\boldsymbol{D}$ ($D = 3/2D_z$; $E = \frac{1}{2}(D_x - D_y) = 0$) tensors, with the exception of **1-F** which was modeled using rhombic tensors ($g_x \neq g_y$; $E/D = 0.333$). While axial models of the data for **1-F** produced similar residuals, the rhombic model is consistent with the HFEPR results. The magnetometry data were fitted using either positive or negative D parameters.[8] It was possible in each case to determine unambiguously the sign of D based on the calculated residual R between the models and the data. Since **1-F** was best modeled with $E/D = 0.333$, the sign of D in this case is not meaningful. Models with rhombic $\boldsymbol{g}$- and $\boldsymbol{D}$-tensors for the other complexes were considered; however, the inclusion of rhombicity did not significantly improve the fits. TIP was included as a variable in the model of the susceptibility data for all compounds. For complex **2-I**, the incorporation of a small, negative TIP parameter accounting for any excess undetermined diamagnetism improved the data fit in the high temperature (>150 K) region as well as the model's parameter precision and was therefore included in the final model. The model for the susceptibility data of **2-I** also includes a Weiss constant (zJ) to account for very small intermolecular spin−spin interactions.

Spectroscopic Methods. UV−vis absorption spectra were measured at room temperature in solution with an Agilent Cary Series UV−vis−NIR spectrophotometer. Infrared spectra were measured on solid-state samples using a Nicolet iS50 FTIR spectrometer. ^{1}H NMR spectra were collected at room temperature using a Varian 400 MHz spectrometer. HFEPR experiments were performed using a transmission spectrometer modified by the incorporation of sources from Virginia Diodes Inc. (VDI, Charlottesville, VA), which generate sub-THz wave radiation in the 50−640 GHz frequency range.[94] The spectrometer is paired with a 15/17-T warm-bore superconducting magnet. FIRMS experiments were performed at the National High Magnetic Field Laboratory using a Bruker Vertex 80v FT-IR spectrometer coupled with a 17 T vertical-bore superconducting magnet in a Voigt configuration. The propagation of light is perpendicular to the external magnetic field. The broadband terahertz radiation emitted by a Hg arc lamp is transmitted through the sample and detected by a composite silicon bolometer (Infrared Laboratories) mounted at the end of the quasi-optical transmission line. Both the sample and bolometer are cooled by low-pressure helium gas to a temperature of 5.5 K. The spectral intensity of each microcrystalline powder sample (∼7 mg, bonded by *n*-eicosane) was measured in the region between 14 and 730 cm^{-1} (0.42−22 THz) with a resolution of 0.3 cm^{-1} (9 GHz). To discern magnetic absorptions from nonmagnetic vibrational absorption features, spectra were normalized by dividing with the reference spectrum, which is the average spectrum collected at all magnetic fields. These normalized transmittance spectra are sensitive to intensity changes induced by the magnetic field. Analysis of the combined HFEPR and FIRMS data was performed using custom MATLAB code and the EPR simulation software package EasySpin.[95]

Computational Methods. DFT and *ab initio* calculations were carried out using the ORCA software package (version 4.0) developed by Dr. F. Neese (MPI-KoFo).[96,97] Computational models were derived from the crystallographic structures. Scalar relativistic effects were accounted for using the ZORA approximation.[98] Calculations employed the valence triple-ζ Karlsruhe basis set recontracted for ZORA with polarization functions on main-group and transition-metal elements (ZORA-def2-TZVP).[99] Single-point calculations and geometry optimizations employed Becke's three-parameter hybrid functional for exchange and the Lee−Yang−Parr correlation functional (B3LYP).[100,101] The resolution of identity and chain of sphere (RIJCOSX) approximations[102] were applied with the appropriate auxiliary basis sets[103] to speed up calculations. The unrestricted natural orbitals provided by the DFT calculations served as the initial guess for state-averaged CASSCF calculations. The CAS(7,5) active space consisted of seven electrons in the five Co 3d orbitals; 10 quartet and 40 doublet states of the d^7 configuration were calculated. The core orbitals were not frozen. Dynamic electron correction was incorporated through *N*-electron valence state second-order perturbation theory (NEVPT2).[104] The multi-configurational CASSCF wavefunctions and NEVPT2-adjusted energies were then used to compute spin-Hamiltonian parameters (g-values and ZFS). EPR g-values for all complexes were computed using the effective Hamiltonian method.[85,105] Both second-order perturbation theory[106] and the effective Hamiltonian approach were used to calculate D and E values for the **1-X** and **2-X** series. *Ab initio* LFT (AILFT)[13,82] yielded relative energies for the Co 3d orbitals based on the CASSCF/NEVPT2 calculations. In addition, electronic structure analysis was performed using the AOM, as implemented in the custom-made programs DDN and DDNFIT (available from J. Telser). The program Ligfield (J. Bendix, Copenhagen U., Denmark) was also used for further comparisons.

■ ASSOCIATED CONTENT

Supporting Information

The Supporting Information is available free of charge at https://pubs.acs.org/doi/10.1021/acs.inorgchem.2c04468.

Single-crystal X-ray diffraction parameters, AOM parameters, computed ZFS parameters, metric parameters of geometry-optimized models, fits and analysis of magnetic susceptibility data, HFEPR spectra of **1-Br** and **1-I**, field vs frequency HFEPR plots for the **2-X** series, additional FIRMS data, UV−vis−NIR absorption spectra for the **2-X** series, computed absorption spectra, and **D**-tensor orientations (PDF)

Accession Codes

CCDC 2226822−2226826 and 2244005−2244006 contain the supplementary crystallographic data for this paper. These data can be obtained free of charge via www.ccdc.cam.ac.uk/data_request/cif, or by emailing data_request@ccdc.cam.ac.uk, or by contacting The Cambridge Crystallographic Data Centre, 12 Union Road, Cambridge CB2 1EZ, UK; fax: +44 1223 336033.

■ AUTHOR INFORMATION

Corresponding Authors

Joshua Telser − *Department of Biological, Physical and Health Sciences, Roosevelt University, Chicago, Illinois 60605, United States;* orcid.org/0000-0003-3307-2556; Email: jtelser@roosevelt.edu; Fax: (+1) 312 341 4358

Adam T. Fiedler − *Department of Chemistry, Marquette University, Milwaukee, Wisconsin 53201, United States;* orcid.org/0000-0002-6114-8557; Email: adam.fiedler@marquette.edu; Fax: (+1) 414-288-7066

Authors

Laxmi Devkota − *Department of Chemistry, Marquette University, Milwaukee, Wisconsin 53201, United States*

Daniel J. SantaLucia − *Department of Chemistry, University of Wisconsin−Madison, Madison, Wisconsin 53706, United States;* Present Address: Max-Planck-Institut für Kohlenforschung, Kaiser-Wilhelm-Platz 1, 45470, Mülheim an der Ruhr, Germany; orcid.org/0000-0002-4201-6612

Amelia M. Wheaton − *Department of Chemistry, University of Wisconsin−Madison, Madison, Wisconsin 53706, United States;* orcid.org/0000-0002-7743-9922

Alexander J. Pienkos − *Department of Chemistry, Marquette University, Milwaukee, Wisconsin 53201, United States*

Sergey V. Lindeman − *Department of Chemistry, Marquette University, Milwaukee, Wisconsin 53201, United States*

https://doi.org/10.1021/acs.inorgchem.2c04468
Inorg. Chem. 2023, 62, 5984−6002

J. Krzystek − *National High Magnetic Field Laboratory, Florida State University, Tallahassee, Florida 32310, United States;* orcid.org/0000-0001-6088-1936

Mykhaylo Ozerov − *National High Magnetic Field Laboratory, Florida State University, Tallahassee, Florida 32310, United States;* orcid.org/0000-0002-5470-1158

John F. Berry − *Department of Chemistry, University of Wisconsin−Madison, Madison, Wisconsin 53706, United States;* orcid.org/0000-0002-6805-0640

Complete contact information is available at: https://pubs.acs.org/10.1021/acs.inorgchem.2c04468

Author Contributions

#L.D. and D.J.S. contributed equally.

Notes

The authors declare no competing financial interest.

■ ACKNOWLEDGMENTS

The authors are grateful for financial support from the U.S. National Science Foundation (CHE-1900562 to A.T.F. and CHE-1953924 to J.F.B.). Part of this work was performed at the National High Magnetic Field Laboratory (NHMFL), which is supported by National Science Foundation Cooperative Agreement no. DMR-1644779 and the State of Florida. The authors thank Dr. A. Ozarowski (NHMFL) for access to his EPR simulation and fitting software and Prof. Jesper Bendix (Copenhagen U., Denmark) for the LFT program Ligfield. D.J.S. received support from the Max-Planck-Gesellschaft and Max-Planck-Institut für Kohlenforschung. L.D. thanks Marquette University for an Eisch Fellowship. The authors also thank an expert reviewer for providing an alternative analysis of the electronic absorption spectra using AILFT, as well as other valuable comments and suggestions.

■ REFERENCES

(1) Terris, B. D.; Thomson, T. Nanofabricated and self-assembled magnetic structures as data storage media. *J. Phys. D: Appl. Phys.* **2005**, *38*, R199−R222.

(2) Leuenberger, M. N.; Loss, D. Quantum computing in molecular magnets. *Nature* **2001**, *410*, 789−793.

(3) Sessoli, R.; Gatteschi, D.; Caneschi, A.; Novak, M. A. Magnetic bistability in a metal-ion cluster. *Nature* **1993**, *365*, 141−143.

(4) Feng, M.; Tong, M.-L. Single Ion Magnets from 3d to 5f: Developments and Strategies. *Chem.—Eur. J.* **2018**, *24*, 7574−7594.

(5) Zabala-Lekuona, A.; Seco, J. M.; Colacio, E. Single-Molecule Magnets: From Mn_{12}-ac to dysprosium metallocenes, a travel in time. *Coord. Chem. Rev.* **2021**, *441*, 213984.

(6) Gómez-Coca, S.; Aravena, D.; Morales, R.; Ruiz, E. Large magnetic anisotropy in mononuclear metal complexes. *Coord. Chem. Rev.* **2015**, *289*−*290*, 379−392.

(7) Whangbo, M.-H.; Xiang, H.; Koo, H.-J.; Gordon, E. E.; Whitten, J. L. Electronic and Structural Factors Controlling the Spin Orientations of Magnetic Ions. *Inorg. Chem.* **2019**, *58*, 11854−11874.

(8) Boča, R. Zero-field splitting in metal complexes. *Coord. Chem. Rev.* **2004**, *248*, 757−815.

(9) Krzystek, J.; Telser, J. Measuring giant anisotropy in paramagnetic transition metal complexes with relevance to single-ion magnetism. *Dalton Trans.* **2016**, *45*, 16751−16763.

(10) Bar, A. K.; Pichon, C.; Sutter, J.-P. Magnetic anisotropy in two- to eight-coordinated transition-metal complexes: Recent developments in molecular magnetism. *Coord. Chem. Rev.* **2016**, *308*, 346−380.

(11) Boča, R.; Rajnak, C. Unexpected behavior of single ion magnets. *Coord. Chem. Rev.* **2021**, *430*, 213657.

(12) Neese, F.; Pantazis, D. A. What is not required to make a single molecule magnet. *Faraday Discuss.* **2011**, *148*, 229−238.

(13) Atanasov, M.; Aravena, D.; Suturina, E.; Bill, E.; Maganas, D.; Neese, F. First principles approach to the electronic structure, magnetic anisotropy and spin relaxation in mononuclear 3d-transition metal single molecule magnets. *Coord. Chem. Rev.* **2015**, *289*−*290*, 177−214.

(14) Schweinfurth, D.; Krzystek, J.; Atanasov, M.; Klein, J.; Hohloch, S.; Telser, J.; Demeshko, S.; Meyer, F.; Neese, F.; Sarkar, B. Tuning Magnetic Anisotropy Through Ligand Substitution in Five-Coordinate Co(II) Complexes. *Inorg. Chem.* **2017**, *56*, 5253−5265.

(15) Suturina, E. A.; Maganas, D.; Bill, E.; Atanasov, M.; Neese, F. Magneto-Structural Correlations in a Series of Pseudotetrahedral $[Co^{II}(XR)_4]^{2-}$ Single Molecule Magnets: An ab Initio Ligand Field Study. *Inorg. Chem.* **2015**, *54*, 9948−9961.

(16) Goodwin, C. A. P. Blocking like it's hot: a synthetic chemists' path to high-temperature lanthanide single molecule magnets. *Dalton Trans.* **2020**, *49*, 14320−14337.

(17) Pyykkö, P. Relativistic effects in chemistry: More common than you thought. *Annu. Rev. Phys. Chem.* **2012**, *63*, 45−64.

(18) Dunn, T. M. Spin-orbit coupling in the first and second transition series. *Trans. Faraday Soc* **1961**, *57*, 1441−1444.

(19) Vijayakumar, M.; Gopinathan, M. S. Spin-orbit coupling constants of transition metal atoms and ions in density functional theory. *J. Mol. Struct.: THEOCHEM* **1996**, *361*, 15−19.

(20) Atanasov, M.; Rauzy, C.; Baettig, P.; Daul, C. Calculation of spin-orbit coupling within the LFDFT: applications to $[NiX_4]^{2-}$ (X = F^-,Cl^-,Br^-,I^-). *Int. J. Quantum Chem.* **2005**, *102*, 119−131.

(21) Koziar, J. C.; Cowan, D. O. Photochemical heavy-atom effects. *Acc. Chem. Res.* **1978**, *11*, 334−341.

(22) Coste, S. C.; Pearson, T. J.; Freedman, D. E. Magnetic Anisotropy in Heterobimetallic Complexes. *Inorg. Chem.* **2019**, *58*, 11893−11902.

(23) Guo, F.-S.; Bar, A. K.; Layfield, R. A. Main Group Chemistry at the Interface with Molecular Magnetism. *Chem. Rev.* **2019**, *119*, 8479−8505.

(24) Duboc, C. Determination and prediction of the magnetic anisotropy of Mn ions. *Chem. Soc. Rev.* **2016**, *45*, 5834−5847.

(25) Duboc, C.; Phoeung, T.; Zein, S.; Pecaut, J.; Collomb, M.-N.; Neese, F. Origin of the Zero-Field Splitting in Mononuclear Octahedral Dihalide Mn^{II} Complexes: An Investigation by Multifrequency High-Field Electron Paramagnetic Resonance and Density Functional Theory. *Inorg. Chem.* **2007**, *46*, 4905−4916.

(26) Zein, S.; Duboc, C.; Lubitz, W.; Neese, F. A Systematic Density Functional Study of the Zero-Field Splitting in Mn(II) Coordination Compounds. *Inorg. Chem.* **2008**, *47*, 134−142.

(27) Wang, L.; Zlatar, M.; Vlahovic, F.; Demeshko, S.; Philouze, C.; Molton, F.; Gennari, M.; Meyer, F.; Duboc, C.; Gruden, M. Experimental and Theoretical Identification of the Origin of Magnetic Anisotropy in Intermediate Spin Iron(III) Complexes. *Chem.—Eur. J.* **2018**, *24*, 5091−5094.

(28) Brazzolotto, D.; Gennari, M.; Yu, S.; Pécaut, J.; Rouzières, M.; Clérac, R.; Orio, M.; Duboc, C. An Experimental and Theoretical Investigation on Pentacoordinated Cobalt(III) Complexes with an Intermediate S = 1 Spin State: How Halide Ligands Affect their Magnetic Anisotropy. *Chem.—Eur. J.* **2016**, *22*, 825−933.

(29) Desrochers, P. J.; Telser, J.; Zvyagin, S. A.; Ozarowski, A.; Krzystek, J.; Vicic, D. A. Electronic Structure of Four-Coordinate C_{3v} Nickel(II) Scorpionate Complexes: Investigation by High-Frequency and High-Field Electron Paramagnetic Resonance and Electronic Absorption Spectroscopies. *Inorg. Chem.* **2006**, *45*, 8930−8941.

(30) Karunadasa, H. I.; Arquero, K. D.; Berben, L. A.; Long, J. R. Enhancing the Magnetic Anisotropy of Cyano-Ligated Chromium(II) and Chromium(III) Complexes via Heavy Halide Ligand Effects. *Inorg. Chem.* **2010**, *49*, 4738−4740.

(31) Stavretis, S. E.; Atanasov, M.; Podlesnyak, A. A.; Hunter, S. C.; Neese, F.; Xue, Z.-L. Magnetic Transitions in Iron Porphyrin Halides by Inelastic Neutron Scattering and Ab Initio Studies of Zero-Field Splittings. *Inorg. Chem.* **2015**, *54*, 9790−9801.

(32) Liu, J.-J.; Meng, Y.-S.; Hlavicka, I.; Orlita, M.; Jiang, S.-D.; Wang, B.-W.; Gao, S. Determination of zero-field splitting in Co^{2+} halide complexes with magnetic and far-IR measurements. *Dalton Trans.* **2017**, *46*, 7408−7411.
(33) Smolko, L.; Cernak, J.; Dusek, M.; Miklovic, J.; Titiš, J.; Boča, R. Three tetracoordinate Co(II) complexes $[Co(biq)X_2]$ (X = Cl, Br, I) with easy-plane magnetic anisotropy as field-induced single-molecule magnets. *Dalton Trans.* **2015**, *44*, 17565−17571.
(34) Bone, A. N.; Widener, C. N.; Moseley, D. H.; Liu, Z.; Lu, Z.; Cheng, Y.; Daemen, L. L.; Ozerov, M.; Telser, J.; Thirunavukkuarasu, K.; Smirnov, D.; Greer, S. M.; Hill, S.; Krzystek, J.; Holldack, K.; Aliabadi, A.; Schnegg, A.; Dunbar, K. R.; Xue, Z.-L. Applying Unconventional Spectroscopies to the Single-Molecule Magnets, $Co(PPh_3)_2X_2$ (X=Cl, Br, I): Unveiling Magnetic Transitions and Spin-Phonon Coupling. *Chem.—Eur. J.* **2021**, *27*, 11110−11125.
(35) Coste, S. C.; Pearson, T. J.; Altman, A. B.; Klein, R. A.; Finney, B. A.; Hu, M. Y.; Alp, E. E.; Vlaisavljevich, B.; Freedman, D. E. Orbital energy mismatch engenders high-spin ground states in heterobimetallic complexes. *Chem. Sci.* **2020**, *11*, 9971−9977.
(36) Coste, S. C.; Vlaisavljevich, B.; Freedman, D. E. Magnetic Anisotropy from Main-Group Elements: Halides versus Group 14 Elements. *Inorg. Chem.* **2017**, *56*, 8195−8202.
(37) Saber, M. R.; Dunbar, K. R. Ligands effects on the magnetic anisotropy of tetrahedral cobalt complexes. *Chem. Commun.* **2014**, *50*, 12266−12269.
(38) Taylor, W. V.; Cashman, B. K.; Xie, Z.-L.; Ngo, K. K.; Rose, M. J. Synthesis and Magnetic Properties of Antimony-Ligated Co(II) Complexes: Stibines versus Phosphines. *Inorg. Chem.* **2022**, *61*, 6733−6741.
(39) Zadrozny, J. M.; Telser, J.; Long, J. R. Slow magnetic relaxation in the tetrahedral cobalt(II) complexes $[Co(EPh)_4]^{2-}$ (E = O, S, Se). *Polyhedron* **2013**, *64*, 209−217.
(40) Yao, X.-N.; Yang, M.-W.; Xiong, J.; Liu, J.-J.; Gao, C.; Meng, Y.-S.; Jiang, S.-D.; Wang, B.-W.; Gao, S. Enhanced magnetic anisotropy in a tellurium-coordinated cobalt single-ion magnet. *Inorg. Chem. Front.* **2017**, *4*, 701−705.
(41) Ona, O. B.; Alcoba, D. R.; Massaccesi, G. E.; Torre, A.; Lain, L.; Melo, J. I.; Oliva-Enrich, J. M.; Peralta, J. E. Magnetic properties of closo-carborane-based Co(II) single-ion complexes with O, S, Se, and Te bridging atoms. *Polyhedron* **2020**, *176*, 114257.
(42) Jiang, S.-D.; Maganas, D.; Levesanos, N.; Ferentinos, E.; Haas, S.; Thirunavukkuarasu, K.; Krzystek, J.; Dressel, M.; Bogani, L.; Neese, F.; Kyritsis, P. Direct Observation of Very Large Zero-Field Splitting in a Tetrahedral $Ni(II)Se_4$ Coordination Complex. *J. Am. Chem. Soc.* **2015**, *137*, 12923−12928.
(43) Ye, S.; Neese, F. How Do Heavier Halide Ligands Affect the Signs and Magnitudes of the Zero-Field Splittings in Halogenonickel(II) Scorpionate Complexes? A Theoretical Investigation Coupled to Ligand-Field Analysis. *J. Chem. Theory Comput.* **2012**, *8*, 2344−2351.
(44) Cahier, B.; Maurice, R.; Bolvin, H.; Mallah, T.; Guihery, N. Tools for predicting the nature and magnitude of magnetic anisotropy in transition metal complexes: application to Co(II) complexes. *Magnetochemistry* **2016**, *2*, 31.
(45) Piwowarska, D.; Gnutek, P.; Rudowicz, C. Origin of the Ground Kramers Doublets for $Co^{2+}(3d^7)$ Ions with the Effective Spin 3/2 Versus the Fictitious "Spin" 1/2. *Appl. Magn. Reson.* **2019**, *50*, 797−808.
(46) Craig, G. A.; Murrie, M. 3d single-ion magnets. *Chem. Soc. Rev.* **2015**, *44*, 2135−2147.
(47) Gómez-Coca, S.; Cremades, E.; Aliaga-Alcalde, N.; Ruiz, E. Mononuclear Single-Molecule Magnets: Tailoring the Magnetic Anisotropy of First-Row Transition-Metal Complexes. *J. Am. Chem. Soc.* **2013**, *135*, 7010−7018.
(48) Murrie, M. Cobalt(II) single-molecule magnets. *Chem. Soc. Rev.* **2010**, *39*, 1986−1995.
(49) Holm, R. H.; Cotton, F. A. Magnetic investigations of spin-free cobaltous complexes. I. Tetrahalocobalt(II) ions. *J. Chem. Phys.* **1959**, *31*, 788−792.
(50) Marts, A. R.; Greer, S. M.; Whitehead, D. R.; Woodruff, T. M.; Breece, R. M.; Shim, S. W.; Oseback, S. N.; Papish, E. T.; Jacobsen, F. E.; Cohen, S. M.; Tierney, D. L. Dual Mode EPR Studies of a Kramers ion: High-Spin Co(II) in 4-, 5-, and 6-Coordination. *Appl. Magn. Reson.* **2011**, *40*, 501−511.
(51) Marts, A. R.; Kaine, J. C.; Baum, R. R.; Clayton, V. L.; Bennett, J. R.; Cordonnier, L. J.; McCarrick, R.; Hasheminasab, A.; Crandall, L. A.; Ziegler, C. J.; Tierney, D. L. Paramagnetic Resonance of Cobalt(II) Trispyrazolylmethanes and Counterion Association. *Inorg. Chem.* **2017**, *56*, 618−626.
(52) Myers, W. K.; Duesler, E. N.; Tierney, D. L. Integrated Paramagnetic Resonance of High-Spin Co(II) in Axial Symmetry: Chemical Separation of Dipolar and Contact Electron-Nuclear Couplings. *Inorg. Chem.* **2008**, *47*, 6701−6710.
(53) Jacobsen, F. E.; Breece, R. M.; Myers, W. K.; Tierney, D. L.; Cohen, S. M. Model Complexes of Cobalt-Substituted Matrix Metalloproteinases: Tools for Inhibitor Design. *Inorg. Chem.* **2006**, *45*, 7306−7315.
(54) Kumar, P.; SantaLucia, D. J.; Kaniewska-Laskowska, K.; Lindeman, S. V.; Ozarowski, A.; Krzystek, J.; Ozerov, M.; Telser, J.; Berry, J. F.; Fiedler, A. T. Probing the Magnetic Anisotropy of Co(II) Complexes Featuring Redox-Active Ligands. *Inorg. Chem.* **2020**, *59*, 16178−16193.
(55) Baum, R. R.; James, C. D.; Tierney, D. L. Paramagnetic resonance of high-spin Co(II) in biologically-relevant environments: models to metalloproteins. *Biol. Magn. Reson.* **2017**, *33*, 33−54.
(56) Aitha, M.; Marts, A. R.; Bergstrom, A.; Møller, A. J.; Moritz, L.; Turner, L.; Nix, J. C.; Bonomo, R. A.; Page, R. C.; Tierney, D. L.; Crowder, M. W. Biochemical, Mechanistic, and Spectroscopic Characterization of Metallo-β-lactamase VIM-2. *Biochemistry* **2014**, *53*, 7321−7331.
(57) Telser, J.; Ozarowski, A.; Krzystek, J. High-frequency and -field electron paramagnetic resonance of transition metal ion (d block) coordination complexes. *Electron Paramagn. Reson.* **2013**, *23*, 209−263.
(58) Krzystek, J.; Ozarowski, A.; Telser, J. Multi-frequency, high-field EPR as a powerful tool to accurately determine zero-field splitting in high-spin transition metal coordination complexes. *Coord. Chem. Rev.* **2006**, *250*, 2308−2324.
(59) Krzystek, J.; Zvyagin, S. A.; Ozarowski, A.; Fiedler, A. T.; Brunold, T. C.; Telser, J. Definitive Spectroscopic Determination of Zero-Field Splitting in High-Spin Cobalt(II). *J. Am. Chem. Soc.* **2004**, *126*, 2148−2155.
(60) Vongtragool, S.; Gorshunov, B.; Dressel, M.; Krzystek, J.; Eichhorn, D. M.; Telser, J. Direct Observation of Fine Structure Transitions in a Paramagnetic Nickel(II) Complex Using Far-Infrared Magnetic Spectroscopy: A New Method for Studying High-Spin Transition Metal Complexes. *Inorg. Chem.* **2003**, *42*, 1788−1790.
(61) Switlicka, A.; Machura, B.; Penkala, M.; Bienko, A.; Bienko, D. C.; Titiš, J.; Rajnak, C.; Boča, R.; Ozarowski, A.; Ozerov, M. Slow Magnetic Relaxation in Cobalt(II) Field-Induced Single-Ion Magnets with Positive Large Anisotropy. *Inorg. Chem.* **2018**, *57*, 12740−12755.
(62) Uehara, K.; Hikichi, S.; Akita, M. Highly labile cationic tris-acetonitrile complexes, $[Tp^RM(NCMe)_3]OTf$ (M = Ni, Co; Tp^R: hydrotrispyrazolylborato, R = Ph, Me and iPr_2): versatile precursors for Tp^R-containing nickel and cobalt complexes. *J. Chem. Soc., Dalton Trans.* **2002**, 3529−3538.
(63) Krzystek, J.; Swenson, D. C.; Zvyagin, S. A.; Smirnov, D.; Ozarowski, A.; Telser, J. Cobalt(II) "Scorpionate" Complexes as Models for Cobalt-Substituted Zinc Enzymes: Electronic Structure Investigation by High-Frequency and Field Electron Paramagnetic Resonance Spectroscopy. *J. Am. Chem. Soc.* **2010**, *132*, 5241−5253.
(64) Yang, L.; Powell, D. R.; Houser, R. P. Structural variation in copper(I) complexes with pyridylmethylamide ligands: structural analysis with a new four-coordinate geometry index, $\tau 4$. *Dalton Trans.* **2007**, 955−964.
(65) Huang, J.; Lee, L.; Haggerty, B. S.; Rheingold, A. L.; Walters, M. A. Hydrotris(3,4-diphenyl-5-methylpyrazol-1-yl)borate: Control of

https://doi.org/10.1021/acs.inorgchem.2c04468
Inorg. Chem. 2023, 62, 5984−6002

Coordination Number via an Equatorial Substituent. *Inorg. Chem.* **1995**, *34*, 4268−4270.
(66) Reinaud, O. M.; Rheingold, A. L.; Theopold, K. H. [Hydrotris(3-isopropyl-5-methylpyrazolyl)borato]iodocobalt(II): Unusual Purification by "Inverse Recrystallization". *Inorg. Chem.* **1994**, *33*, 2306−2308.
(67) Sirianni, E. R.; Cummins, D. C.; Yap, G. P. A.; Theopold, K. H. FcTp(R) (R = ^{i}Pr or ^{t}Bu): third-generation ferrocenyl scorpionates. *Acta Crystallogr., Sect. C: Struct. Chem.* **2016**, *72*, 813−818.
(68) Gorrell, I. B.; Parkin, G. (Tris-(3-tert-butylpyrazolyl)-hydroborato)manganese(II), -iron(II), -cobalt(II), and -nickel(II) halide derivatives: facile abstraction of fluoride from tetrafluoroborate-(1-). *Inorg. Chem.* **1990**, *29*, 2452−2456.
(69) Jove, F. A.; Pariya, C.; Scoblete, M.; Yap, G. P. A.; Theopold, K. H. A Family of Four-Coordinate Iron(II) Complexes Bearing the Sterically Hindered Tris(pyrazolyl)borato Ligand $Tp^{tBu,Me}$. *Chem.—Eur. J.* **2011**, *17*, 1310−1318.
(70) Rauch, M.; Rong, Y.; Sattler, W.; Parkin, G. Synthesis of a terminal zinc hydride compound, $[Tp^{But,Me}]ZnH$, from a hydroxide derivative, $[Tp^{But,Me}]ZnOH$: Interconversions with the fluoride complex, $[Tp^{But,Me}]ZnF$. *Polyhedron* **2016**, *103*, 135−140.
(71) Yoon, K.; Parkin, G.; Rheingold, A. L. A reinvestigation of the molecular structures of cis-mer-$MoOCl_2(PR_3)_3$: do bond-stretch isomers really exist? *J. Am. Chem. Soc.* **1991**, *113*, 1437−1438.
(72) Addison, A. W.; Rao, T. N.; Reedijk, J.; Vanrijn, J.; Verschoor, G. C. Synthesis, structure, and spectroscopic properties of copper(II) compounds containing nitrogen−sulphur donor ligands; the crystal and molecular structure of aqua[1,7-bis(N-methylbenzimidazol-2′-yl)-2,6-dithiaheptane]copper(II) perchlorate. *J. Chem. Soc., Dalton Trans.* **1984**, 1349−1356.
(73) Green, W. L.; Sirianni, E. R.; Yap, G. P. A.; Riordan, C. G. Steric and electronic factor comparisons in hydrotris(3-phenylpyrazolyl)borate nickel(II) aryloxides. *Acta Crystallogr., Sect. C: Struct. Chem.* **2016**, *72*, 791−796.
(74) Rudowicz, C.; Karbowiak, M. Disentangling intricate web of interrelated notions at the interface between the physical (crystal field) Hamiltonians and the effective (spin) Hamiltonians. *Coord. Chem. Rev.* **2015**, *287*, 28−63.
(75) Papankova, B.; Boča, R.; Dlhan, L.; Nemec, I.; Titiš, J.; Svoboda, I.; Fuess, H. Magneto-structural relationships for a mononuclear Co(II) complex with large zero-field splitting. *Inorg. Chim. Acta* **2010**, *363*, 147−156.
(76) Krzystek, J.; Zvyagin, S. A.; Ozarowski, A.; Trofimenko, S.; Telser, J. Tunable-frequency high-field electron paramagnetic resonance. *J. Magn. Reson.* **2006**, *178*, 174−183.
(77) Moseley, D. H.; Stavretis, S. E.; Thirunavukkuarasu, K.; Ozerov, M.; Cheng, Y.; Daemen, L. L.; Ludwig, J.; Lu, Z.; Smirnov, D.; Brown, C. M.; Pandey, A.; Ramirez-Cuesta, A. J.; Lamb, A. C.; Atanasov, M.; Bill, E.; Neese, F.; Xue, Z. L. Spin-phonon couplings in transition metal complexes with slow magnetic relaxation. *Nat. Commun.* **2018**, *9*, 2572.
(78) Kragskow, J. G. C.; Marbey, J.; Buch, C. D.; Nehrkorn, J.; Ozerov, M.; Piligkos, S.; Hill, S.; Chilton, N. F. Analysis of vibronic coupling in a 4f molecular magnet with FIRMS. *Nat. Commun.* **2022**, *13*, 825.
(79) Plugis, N. M.; Rudd, N. D.; Krzystek, J.; Swenson, D. C.; Telser, J.; Larrabee, J. A. Cobalt(II) "Scorpionate" complexes as electronic ground state models for cobalt-substituted zinc enzymes: Structure investigation by magnetic circular dichroism. *J. Inorg. Biochem.* **2020**, *203*, 110876.
(80) Mossin, S.; Weihe, H.; Barra, A.-L. Is the Axial Zero-Field Splitting Parameter of Tetragonally Elongated High-Spin Manganese-(III) Complexes Always Negative? *J. Am. Chem. Soc.* **2002**, *124*, 8764−8765.
(81) Brorson, M.; Schaeffer, C. E. Orthonormal interelectronic repulsion operators in the parametrical dq model. Application of the model to gaseous ions. *Inorg. Chem.* **1988**, *27*, 2522−2530.
(82) Atanasov, M.; Ganyushin, D.; Pantazis, D. A.; Sivalingam, K.; Neese, F. Detailed Ab Initio First-Principles Study of the Magnetic Anisotropy in a Family of Trigonal Pyramidal Iron(II) Pyrrolide Complexes. *Inorg. Chem.* **2011**, *50*, 7460−7477.
(83) Schweinfurth, D.; Sommer, M. G.; Atanasov, M.; Demeshko, S.; Hohloch, S.; Meyer, F.; Neese, F.; Sarkar, B. The Ligand Field of the Azido Ligand: Insights into Bonding Parameters and Magnetic Anisotropy in a Co(II)-Azido Complex. *J. Am. Chem. Soc.* **2015**, *137*, 1993−2005.
(84) Deb, T.; Anderson, C. M.; Ma, H.; Petersen, J. L.; Young, V. G., Jr.; Jensen, M. P. Scorpionato Halide Complexes $[(Tp^{Ph,Me})Ni\text{-}X]$ [X = Cl, Br, I; $Tp^{Ph,Me}$ = Hydrotris(3-phenyl-5-methyl-1-pyrazolyl)-borate]: Structures, Spectroscopy, and Pyrazole Adducts. *Eur. J. Inorg. Chem.* **2015**, *2015*, 458−467.
(85) Singh, S. K.; Eng, J.; Atanasov, M.; Neese, F. Covalency and chemical bonding in transition metal complexes: An ab initio based ligand field perspective. *Coord. Chem. Rev.* **2017**, *344*, 2−25.
(86) Puerta, D. T.; Cohen, S. M. $[(Tp^{Me,Ph})_2Zn_2(H_3O_2)]ClO_4$: a new H_3O_2 species relevant to zinc proteinases. *Inorg. Chim. Acta* **2002**, *337*, 459−462.
(87) Trofimenko, S.; Calabrese, J. C.; Kochi, J. K.; Wolowiec, S.; Hulsbergen, F. B.; Reedijk, J. Spectroscopic analysis, coordination geometry, and x-ray structures of nickel(II) compounds with sterically demanding tris(pyrazolyl)borate ligands and azide or (thio)cyanate anions. Crystal and molecular structures of bis[(μ-thiocyanato-N,S)(hydrotris(3-isopropyl-4-bromopyrazol-1-yl)borato)nickel(II)]-3-heptane and (thiocyanato-N)(hydrotris(3-tert-butyl-5-methylpyrazol-1-yl)borato)nickel(II). *Inorg. Chem.* **1992**, *31*, 3943−3950.
(88) Bourhis, L. J.; Dolomanov, O. V.; Gildea, R. J.; Howard, J. A. K.; Puschmann, H. The anatomy of a comprehensive constrained, restrained refinement program for the modern computing environment—Olex2 dissected. *Acta Crystallogr., Sect. A: Found. Adv.* **2015**, *71*, 59−75.
(89) Sheldrick, G. M. Crystal structure refinement with SHELXL. *Acta Crystallogr., Sect. C: Struct. Chem.* **2015**, *71*, 3−8.
(90) Wang, G. F.; Zhang, X.; Sun, S. W.; Sun, H.; Ma, H. X. Synthesis and structural characterization of two half-sandwich nickel(II) complexes with the scorpionate ligands. *Crystallogr. Rep.* **2015**, *60*, 1032−1037.
(91) Bain, G. A.; Berry, J. F. Diamagnetic corrections and Pascal's constants. *J. Chem. Educ.* **2008**, *85*, 532−536.
(92) Chilton, N. F.; Anderson, R. P.; Turner, L. D.; Soncini, A.; Murray, K. S. PHI: A powerful new program for the analysis of anisotropic monomeric and exchange-coupled polynucleard- andf-block complexes. *J. Comput. Chem.* **2013**, *34*, 1164−1175.
(93) Bill, E. *JulX20*, version 1.4; Max-Planck-Institute für Chemische Energiekonversion.
(94) Hassan, A. K.; Pardi, L. A.; Krzystek, J.; Sienkiewicz, A.; Goy, P.; Rohrer, M.; Brunel, L. C. Ultrawide Band Multifrequency High-Field EMR Technique: A Methodology for Increasing Spectroscopic Information. *J. Magn. Reson.* **2000**, *142*, 300−312.
(95) Stoll, S.; Schweiger, A. EasySpin, a comprehensive software package for spectral simulation and analysis in EPR. *J. Magn. Reson.* **2006**, *178*, 42−55.
(96) Neese, F. *ORCA—An Ab Initio, DFT and Semiempirical Electronic Structure Package*, version 4.0; Max Planck Institute for Chemical Energy Conversion: Muelheim (Germany), 2017.
(97) Neese, F. The ORCA program system. *Wiley Interdiscip. Rev.: Comput. Mol. Sci.* **2012**, *2*, 73−78.
(98) van Lenthe, E.; Baerends, E. J.; Snijders, J. G. Relativistic total energy using regular approximations. *J. Chem. Phys.* **1994**, *101*, 9783−9792.
(99) Weigend, F.; Ahlrichs, R. Balanced basis sets of split valence, triple zeta valence and quadruple zeta valence quality for H to Rn: Design and assessment of accuracy. *Phys. Chem. Chem. Phys.* **2005**, *7*, 3297−3305.
(100) Becke, A. D. Density functional thermochemistry. III. The role of exact exchange. *J. Chem. Phys.* **1993**, *98*, 5648−5652.
(101) Lee, C. T.; Yang, W. T.; Parr, R. G. Development of the Colle-Salvetti correlation-energy formula into a functional of the electron density. *Phys. Rev. B* **1988**, *37*, 785−789.

https://doi.org/10.1021/acs.inorgchem.2c04468
Inorg. Chem. 2023, 62, 5984−6002

(102) Neese, F.; Wennmohs, F.; Hansen, A.; Becker, U. Efficient, approximate and parallel Hartree-Fock and hybrid DFT calculations. A "chain-of-spheres" algorithm for the Hartree-Fock exchange. *Chem. Phys.* **2009**, *356*, 98−109.
(103) Weigend, F. Accurate Coulomb-fitting basis sets for H to Rn. *Phys. Chem. Chem. Phys.* **2006**, *8*, 1057−1065.
(104) Angeli, C.; Cimiraglia, R.; Evangelisti, S.; Leininger, T.; Malrieu, J. P. Introduction of n-electron valence states for multireference perturbation theory. *J. Chem. Phys.* **2001**, *114*, 10252−10264.
(105) Singh, S. K.; Atanasov, M.; Neese, F. Challenges in Multireference Perturbation Theory for the Calculations of the g-Tensor of First-Row Transition-Metal Complexes. *J. Chem. Theory Comput.* **2018**, *14*, 4662−4677.
(106) Neese, F.; Solomon, E. I. Calculation of Zero-Field Splittings, g-Values, and the Relativistic Nephelauxetic Effect in Transition Metal Complexes. Application to High-Spin Ferric Complexes. *Inorg. Chem.* **1998**, *37*, 6568−6582.

https://doi.org/10.1021/acs.inorgchem.2c04468
Inorg. Chem. 2023, 62, 5984−6002